

The Subcortical Atlas of the Rhesus Macaque (SARM) for neuroimaging

Renée Hartig^{a,b,c}, Daniel Glen^d, Benjamin Jung^{e,f}, Nikos K. Logothetis^{b,g,k}, George Paxinos^h, Eduardo A. Garza-Villarreal^{i,*}, Adam Messinger^{f,*}, Henry C. Evrard^{a,b,j,k,*}



^a Centre for Integrative Neurosciences, University of Tübingen, Tübingen, Germany

^b Max Planck Institute for Biological Cybernetics, Tübingen, Germany

^c Department of Psychiatry and Psychotherapy, Central Institute of Mental Health, Medical Faculty Mannheim, Heidelberg University, Mannheim, Germany

^d Scientific and Statistical Computing Core, National Institute of Mental Health, Bethesda, USA

^e Department of Neuroscience, Brown University, Providence, RI, USA

^f Laboratory of Brain and Cognition, National Institute of Mental Health, Bethesda, USA

^g University of Manchester, Manchester, United Kingdom

^h Neuroscience Research Australia and The University of New South Wales, Sydney, NSW 2031, Australia

ⁱ Instituto de Neurobiología, Universidad Nacional Autónoma de México campus Juriquilla, Querétaro, Mexico

^j Nathan S. Kline Institute for Psychiatric Research, Center for Biomedical Imaging and Neuromodulation, Orangeburg, NY, USA

^k International Center for Primate Brain Research, Songjiang, Shanghai, PR China

ARTICLE INFO

Keywords:

Segmentation
Anatomy
Subcortex
Cerebellum
Thalamus
Brainstem

ABSTRACT

Digitized neuroanatomical atlases that can be overlaid onto functional data are crucial for localizing brain structures and analyzing functional networks identified by neuroimaging techniques. To aid in functional and structural data analysis, we have created a comprehensive parcellation of the rhesus macaque subcortex using a high-resolution *ex vivo* structural imaging scan. This anatomical scan and its parcellation were warped to the updated NIMH Macaque Template (NMT v2), an *in vivo* population template, where the parcellation was refined to produce the Subcortical Atlas of the Rhesus Macaque (SARM) with 210 primary regions-of-interest (ROIs). The subcortical parcellation and nomenclature reflect those of the 4th edition of the Rhesus Monkey Brain in Stereotaxic Coordinates (Paxinos et al., *in preparation*), rather than proposing yet another novel atlas. The primary ROIs are organized across six spatial hierarchical scales from small, fine-grained ROIs to broader composites of multiple ROIs, making the SARM suitable for analysis at different resolutions and allowing broader labeling of functional signals when more accurate localization is not possible. As an example application of this atlas, we have included a functional localizer for the dorsal lateral geniculate (DLG) nucleus in three macaques using a visual flickering checkerboard stimulus, identifying and quantifying significant fMRI activation in this atlas region. The SARM has been made openly available to the neuroimaging community and can easily be used with common MRI data processing software, such as AFNI, where the atlas has been embedded into the software alongside cortical macaque atlases.

1. Introduction

As functional magnetic resonance imaging (fMRI) and positron emission tomography (PET) continue to advance spatiotemporal resolution limits, there is a growing opportunity for researchers to examine subcortical regions and their involvement in cortico-subcortical networks. The smaller subcortical regions have, however, largely been absent from digitized atlases for non-human primate (NHP) neuroimaging. In contrast to human research, where several subcortical atlases exist, NHP

researchers typically have to employ workarounds and parcellate individual regions-of-interest (ROIs) themselves. To address this void, we present the Subcortical Atlas of the Rhesus Macaque (SARM), a MRI-based digital subcortical atlas offering a standardized parcellation for ROI and network analyses.

The development of the SARM is timely. While previously used in only a few primate research centers, fMRI is now being employed in many NHP laboratories (Milham et al., 2018). The use of contrast agents, improved sequences, and high-field magnets has increased the signal-to-noise ratio and spatial resolution of neuroimaging; such advances facil-

Abbreviations: fMRI, functional Magnetic Resonance Imaging; DLG, Dorsal Lateral Geniculate; NHP, non-human primate; NMT v2, NIMH Macaque Template version 2; RMBSC4, 4th edition of the Rhesus Monkey Brain in Stereotaxic Coordinates; ROIs, regions of interest; SARM, Subcortical Atlas of the Rhesus Macaque; CHARM, Cortical Hierarchy Atlas of the Rhesus Macaque.

* Corresponding authors.

E-mail addresses: Henry.Evrard@nki.rfmh.org (H.C. Evrard), adam.messinger@nih.gov (A. Messinger), egarza@comunidad.unam.mx (E.A. Garza-Villarreal).

<https://doi.org/10.1016/j.neuroimage.2021.117996>.

Received 16 September 2020; Received in revised form 15 March 2021; Accepted 19 March 2021

Available online 29 March 2021.

1053-8119/© 2021 Published by Elsevier Inc. This is an open access article under the CC BY-NC-ND license (<http://creativecommons.org/licenses/by-nc-nd/4.0/>)

itate reproducible detection of subcortical activations (e.g., Baker et al., 2006; Logothetis et al., 2012; Ortiz-Rios et al., 2015; Quan et al., 2020). Technological improvements in data collection methods have also resulted in greater potential for employing fMRI concurrently with subcortical electrical microstimulation (Logothetis et al., 2010; Arsenault and Vanduffel, 2019; Murris, Arsenault and Vanduffel, 2020), optogenetics (Nassi et al., 2015; Klein et al., 2016; Stauffer et al., 2016), or electrophysiological recordings (Logothetis et al., 2012), all the while capturing the mesoscopic and systems-level effects (see also, Klink et al., this issue). Such studies require fine-grain delineations of the subcortex to aid both in planning stereotaxic implantations and interpreting local signal modulation. Finally, while NHP fMRI still typically relies on two or three subjects, there is a growing interest in using larger groups and applying group analyses (e.g. Fox et al., 2015). The advent of multi-center data sharing (Milham et al., 2018) also allows for the possibility of larger sample sizes, and clearly calls for group-level analyses performed on data aligned to a population brain template with standardized atlases (Milham et al., 2020; Jung et al., this issue).

Previous NHP studies examining subcortical activity have created their own individual masks covering regions known to include specific brainstem nuclei. For example, Logothetis et al. (2012) manually segmented 25 subcortical ROIs for each of their five subjects separately. Noonan et al. (2014) masked the area between the medulla and midbrain for localizing activity from serotonergic nuclei with 0.5 mm spatial resolution. Murris et al. (2020) registered their functional data to the D99 macaque template (Reveley et al., 2017), and then added ROIs for the ventral tegmental area (VTA) and accumbens nucleus (Acb), which were absent in the D99 atlas. Creating individual masks is one strategy to study regional fMRI activity; however, precise delineation of structural boundaries requires high-quality structural scans, a great deal of labor, and anatomical expertise. Furthermore, for comparisons across individuals or group-level analyses, single-subject scans and regional masks must then be nonlinearly registered to a common reference template. While warping of fMRI data to a standard space can be successful for fairly large subcortical parcellations (e.g., the hippocampus, amygdala, and distinguishable midbrain regions; Fox et al., 2015), nonlinear registration of smaller subcortical structures can be a delicate step in the data processing pipeline. The SARM allows for varying alignment and resolution limits, providing groupings of regions at various hierarchically organized spatial scales that are suited for different purposes, including functional neuroimaging studies.

In comparison to the numerous human MRI-based brain atlases (e.g., Damasio 2005; Accolla et al., 2014; Pipitone et al., 2014; Ding et al., 2016; Ewert et al., 2017; Pauli et al., 2018), and despite the existence of NHP paper atlases, including an exhaustive mapping of the subcortex (Paxinos et al., 2009; Martin and Bowden, 2000), limited efforts have been made to digitize the macaque subcortex parcellations. Previous attempts to digitize subcortical parcellations from printed macaque atlases have provided some segmentation of the subcortex. For example, the Saleem and Logothetis (2012) atlas was digitized by alignment to a high-resolution MRI of an ex vivo surrogate (Reveley et al. 2017). However, this digital D99 atlas includes only some subcortical structures (e.g., hippocampus, amygdala, striatum, and claustrum). Likewise, the parcellation of post-mortem macaque brains by Calabrese et al. (2015) contains a detailed segmentation of most telencephalic and diencephalic brain nuclei (Paxinos et al., 2009), but little to no parcellation of the brainstem. The NeuroMaps macaque atlas covers the whole brain and is presented on an ex vivo juvenile rhesus macaque brain (Bakker et al., 2015; Rohlfing et al., 2012). The NeuroMaps segmentation was later refined on the INIA19 adult population *in vivo* symmetric template (Rohlfing et al., 2012). Rohlfing and colleagues noted, however, that their segmentation of the basal forebrain, hypothalamus and amygdala is incomplete and that the internal segmentation of the thalamus, midbrain and hindbrain may not be reliable. Although a more detailed digital subcortical map is needed, there is a fine line between segmenting all the minute cytoarchitectonic subnuclei that can be appreciated in histological prepara-

tions under the microscope and the spatial resolution afforded by structural and functional neuroimaging. Using an updated version of the Rhesus Monkey Brain in Stereotaxic Coordinates histological atlas (Paxinos et al., in preparation; ~500 cytoarchitectonic subcortical regions) for guidance, version 1 of the SARM (SARM v1) presented here proposes a parcellation of the subcortex into 210 primary ROIs. The SARM, thereby, addresses the need for a more comprehensive subcortical segmentation and attempts to strike a practical balance between cytoarchitectonic details and the constraints imposed by the lower anatomical resolution and distortions of MRI.

While *ex vivo* scans, such as the D99 surrogate or the Calabrese *ex vivo* population template (Calabrese et al., 2015), can provide great detail because they are not impacted by animal movement or physiological noise, *in vivo* templates better reflect the living brain's configuration (e.g., with regard to size, ventricle shape, and the presence of cerebrospinal fluid). Atlases drawn on a single subject template can precisely reflect the particular anatomy of that subject, but may not be morphologically representative of the species due to large inter-individual variability. The SARM was fit to version 2 of the NIMH Macaque Template (NMT v2), a high-resolution population template based on *in vivo* scans collected at high field strength (4.7 T) from a large cohort (N=31) of adult rhesus monkeys (Seidlitz et al., 2018; Jung et al., this issue). The NMT v2 compares favorably to the INIA19 template in terms of resolution (0.25 mm vs. 0.50 mm isotropic), allowing for finer parcellation of subcortical structures, and is already home to the Cortical Hierarchy Atlas of the Rhesus Macaque (CHARM; Jung et al., this issue). Because average population templates are representative, most individuals will require relatively little distortion to be aligned to such a template as compared to an *ex vivo* or individual scan (Kochunov et al., 2001; Molfese et al., 2015; Feng et al., 2017). This, in effect, minimizes alignment errors, which are of particular importance for small subcortical nuclei.

To create the SARM, we relied on the high resolution and precision of an *ex vivo* single-subject structural scan and previously obtained histological material to draw the primary structures. These regions were then warped to the symmetric version of the NMT v2, where they were manually refined to reflect the representative anatomy of the population template. The SARM parcellation was then hierarchically grouped into larger composite structures to create ROI clusters suitable for neuroimaging analysis. The SARM is available on various online platforms (PRIME-RE, Zenodo, and AFNI), where it is being continuously improved and further delineated.

2. Materials and methods

2.1. Atlas preparation

2.1.1. Ex vivo anatomical sample

A whole-brain *ex vivo* sample from one adult female rhesus macaque (G12; *Macaca mulatta*; ~8 kg; Table 1) was used as a single-subject anatomical template to parcellate the subcortex. This subject was part of an anatomical study approved by the local authorities and in full compliance with the European Parliament and Council Directive 2010/63/EU. The subject was not involved in any invasive procedures and never underwent intracerebral surgery. After transcardial fixation with 4% formalin (Evraud et al., 2012), the brain was placed into a jar of agar and positioned upright in a horizontal 7T Bruker BioSpec scanner, with the brain oriented parallel to the scanner (dorsal side positioned upward) (Bruker BioSpin, Ettlingen, Germany). The entire brain was scanned using a high-resolution fast low-angle shot (FLASH) sequence (voxel dimensions: 0.15 × 0.15 × 1.0 mm; flip angle: 50°; TR/TE: 2500/9 ms; field-of-view (FOV): 70 × 52 mm; matrix size: 468 × 346; 78 coronal slices).

2.1.2. Segmentation in individual (G12) space

Subcortical ROIs were manually drawn by author HCE onto coronal slices of the G12 high-resolution *ex vivo* anatomical scan using the

Table 1
List of monkey brains used for the preparation of the SARM.

Section	N	Name	Image	Reference
2.1.1	1	G12	MRI FLASH $0.15 \times 0.15 \times 1.0$ mm	present study
2.1.2	2	RMBSC4 (chapters 1 and 2)	Photomicrographs of Nissl, AChE and SMI-32 from 2 brains	Paxinos et al., in preparation
2.1.3/4	31	NMT v2 (average)	T1 population-averaged template 0.25 mm isotropic	Jung et al., this issue

Amira software (Amira 6.0.1; FEI). The fine spatial resolution of the contrast variation in the slices enabled recognizing and mapping discrete anatomical regions identified in corresponding anteroposterior planes in histological sections from 2 monkey brains (Table 1) in the 4th edition of the Rhesus Monkey Brain in Stereotaxic Coordinates (RMBSC4; Paxinos et al., in preparation). These reference sections previously underwent Nissl, SMI-32 and acetylcholinesterase (AChE) staining (Paxinos et al., 2009), and were recently digitized at high-resolution ($0.44 \times 0.44 \mu\text{m}^2$ pixels) using a slide-scanner microscope (AxioScan; Zeiss) for further examination (Paxinos et al., in preparation). In both brains, the staining was made using standard Nissl histology (0.5% cresyl violet), AChE histochemistry (Koelle and Friedenwald, 1949; Lewis, 1961), and SMI-32 immunohistology (1:1000; Covance) using alternate 1-in-10 series of $50 \mu\text{m}$ -thick sections, as described in detail elsewhere (Paxinos et al., 2009; Paxinos et al. in preparation). Despite major improvements and updates, the order of the figures from the 2 monkey brains in the upcoming 4th edition does not differ from the 2nd edition (chapters 1 and 2, in both editions); thus, readers can still refer to the printed 2nd edition of RMBSC (Paxinos et al., 2009) when references to specific figures are made in the text below. The ROIs were drawn on G12 while examining all three stereotaxic planes of G12 to reduce inconsistencies in delineation across slices. Neighboring cytoarchitectonic regions defined in RMBSC4 that were too small, and not clearly discernible from contrast changes in the G12 scan, were englobed together in a single large ROI, as detailed in the Results (Section 3.1). Additional resources included parcellations of the hypothalamus (Ongur et al., 1998; Saper et al., 2012; Wells et al., 2020), thalamus (Olszewski, 1952; Calzavara et al., 2005; Evrard and Craig, 2008; Mai and Forutan, 2012), amygdala (Amaral et al., 1992; Stefanacci et al., 2000), and basal ganglia (Haber et al., 2012) in macaques, as well as in humans when relevant.

2.1.3. Nonlinear registration

The single-subject (G12) *ex vivo* structural scan and subcortical segmentation were nonlinearly registered to the symmetric NMT v2 full-head anatomical template for rhesus macaques. The NMT v2 template (Jung et al., this issue) is in stereotaxic orientation (Horsley and Clarke, 1908; also referred to as the Frankfurt or Ear Bar Zero, EBZ, plane). The subcortical segmentation was refined on a single hemisphere (the left) of the symmetric NMT v2 template and mirrored onto the opposite hemisphere in order to assure that the resulting parcellation has left and right ROIs of equal size.

To coregister the G12 template and atlas to the NMT v2, the NifTI images were first converted to MINC format (<http://www.bic.mni.mcgill.ca/ServicesSoftware/MINC>) and the origin of the spatial coordinates was adjusted to correspond to the intersection of the midsagittal section and the interaural line (i.e., Ear Bar Zero, EBZ). Then, we used *volmatch* and *volflip* (MINC widgets) to reorient the images to the NMT v2. The G12 template was then converted back to NifTI. Using Advanced Normalization Tools (ANTS; version 2.3.1.dev159-gea5a7; Avants et al., 2014), we produced a negative image of the G12 T2-weighted scan, so its contrast would be similar to the T1-weighted NMT v2 template. The G12 template showed air bubble-induced artifacts around the left lateral ventricle that affected registration. To correct these artifacts and improve registration, we manually traced each artifact to the underlying tissue (namely, the putamen) and matched it with the tissue's intensity. This new volume was then corrected for N4 Bias Field artifacts

(Tustison et al., 2010). The ANTs registration pipeline was optimized using an in-house script that employed a custom mask of the subcortex for some of the registration steps. After computing the G12 to NMT v2 template registration, we used *antsApplyTransformation* to nonlinearly coregister the subcortical parcellation to the NMT v2 with Generic Label interpolation.

2.1.4. Refinement of ROIs in the NMT v2 template

The resulting atlas regions suffered from some irregularities stemming from the limitations of the original anisotropic voxels (high resolution within the coronal plane, but coarser resolution across planes) and from the interpolation methods associated with the nonlinear warp of the ROI labels. Therefore, we followed the ANTs-based alignment pipeline with a procedure to spatially regularize regions using AFNI commands. The regions were processed with a modal smoothing technique that replaces each voxel with the most common label in a 1- or 2-voxel spherical neighborhood around every voxel. A select list of thin or small regions were smoothed using the 1 voxel mode, and all other regions were smoothed using the 2 voxel mode. The data were masked by the CSF and blood vessel segmentations from NMT v2. Each ROI was automatically further refined by examining the distribution of voxel intensities in NMT v2. For each ROI, we sampled the voxel intensities of NMT v2 in that ROI, and voxels farther than three standard deviations away from the mean intensity (potentially indicating encroachment of the ROI into a different tissue class) were compared with the 26 adjacent voxels and reassigned to the label of the voxel with the most similar intensity. This outlier detection was performed across ten iterations. The quality of the alignment between the transformed G12 and the NMT v2 template was assessed by viewing the former on the outline of the latter using @chauffeur_afni. Finally, the atlas was assessed for discontinuities, and discontinuous clusters smaller than five percent of the size of the largest portion of the ROI were replaced with labels from neighboring voxels. With the atlas regions now transformed to the NMT v2 symmetric template space, the regions were manually adjusted, again in Amira by author HCE, with reviewing by authors HCE and GP, to reflect the anatomical transitions evident in this population template. Before exporting from AMIRA, a Gaussian smoothing ($2 \times 2 \times 2$ pixel filter mask) was applied across the 3D volume using the “Smooth Labels” function. Following AMIRA export, the SARM regions were modally smoothed with a 1.8 voxel radius and discontinuous clusters smaller than five percent of the size of the largest portion of the ROI were again replaced with labels from neighboring voxels. At each step, volume changes of each ROI were tracked to prevent large, unintended changes to the ROIs.

2.2. Subcortical naming hierarchy

2.2.1. Multi-scale hierarchical grouping

To create composites of primary ROIs at multiple spatial scales, neighboring subcortical ROIs in the primary parcellation (level 6) were iteratively grouped into successively larger composite ROIs. This iterative grouping results into progressively larger and more general anatomical ROIs, organized hierarchically from level 6 (finest parcellation) to level 1 (coarsest parcellation). This hierarchy forms the SARM. In the present work, “hierarchy” does not refer to models of cortical information flow (e.g., Felleman and Van Essen, 1991; Hilgetag and Goulas, 2020), but to the notion of ‘hierarchical organization,’ with one global ROI at the top of the hierarchy (i.e., subcortex at level 0), and pro-

gressively more numerous and smaller ROIs being further subdivided at successive hierarchical levels (levels 1–5; see *Results*).

Thus, the finest level of the SARM hierarchy (level 6) delineates each of our manually drawn, or ‘primary,’ ROIs, which were defined on the basis of the RMBSC4, as described above. Composite regions in levels 5–1 were successively built from smaller adjacent areas in the preceding finer level. While the brain can most broadly be subdivided into the forebrain, midbrain, and hindbrain, level 1 begins with the five developmental (i.e., embryological) sub-divisions of the subcortex, namely the tel-, di-, mes-, met-, and myel-encephalon. The SARM levels 2–4 consist of ROIs of sufficient size to accommodate functional imaging voxels that are typically 1.25–1.50 mm on a side, whereas levels 5–6 ROIs may benefit from the higher resolution of structural imaging. Level 5 was frequently left the same as level 6 (with level 5 being however slightly coarser than level 6; [Table S1](#)) to allow for the potential future parcelation of level 6 regions. However, in select cases where substructure could be appreciated at multiple spatial scales, distinct level 5 regions consisting of multiple level 6 regions were defined. This occurred in regions including the cerebellum, striatum, as well as with subnuclei of the amygdala (e.g., lateral and basal nuclei), rubral region, colliculi, parabrachial complex, and hypothalamus (see *Results* and [Table S1](#)). In most cases, we grouped the ROIs based on their developmental ontology (i.e., hierarchical developmental origin; [Puelles et al., 2013](#)) and/or functional relationships ([Mai and Paxinos, 2012](#); [Puelles et al., 2013](#); see also [Calabrese et al., 2015](#) for a similar approach), with the condition that these ROIs had to be spatially contiguous. In some cases, particularly at coarser levels, ROIs had to be grouped solely based on their spatial proximity, creating functionally heterogeneous composites.

Independent of their hierarchical classification, all ROIs were classified as being primarily subcortical gray matter or white matter. In select instances, ROIs composed primarily of white matter or other tissue types were included in larger composite ROIs to make them whole (e.g. the internal capsule was included in the striatum to bridge the caudate and putamen) and because sparse cell bodies within such white matter regions can lead to their functional activation.

2.2.2. Nomenclature

Each ROI and group of ROIs has a unique full name and abbreviation. At levels 5 and 6, the names and abbreviations of the ROIs typically match those defined in the RMBSC4, with some exceptions (see *Results*) to accommodate the most commonly used naming convention in NHP neuroimaging. At levels 2–4, the names and abbreviations of the groups of ROIs reflect either a common developmental origin (e.g., pallial vs. subpallial amygdala; [Puelles et al., 2013](#)), a classical neuroanatomical grouping (e.g., basal ganglia; [Mai and Paxinos, 2012](#)) or a spatial proximity (e.g., dorsal vs. ventral mesencephalon).

AFNI allows for flexible indexing of ROIs by either index number, abbreviation, or the full name of the ROI. To prevent conflicts between index numbers and names, SARM abbreviations do not start with a number (e.g., the abducens nucleus is abbreviated 6N in RMBSC4 but N6 in SARM). In addition, to maximize compatibility with scripts and programs, abbreviations do not include special characters, and full names use underscores in place of spaces. A full list of the SARM v1 regions is provided in [Table S1](#). A spreadsheet of the hierarchy and full list of SARM structures are also available for download with the NMT v2 package.

2.3. Functional localizer

To illustrate the usefulness of this atlas within the context of fMRI data analysis, a functional localizer for the dorsal lateral geniculate nucleus (DLG) (also referred to as the lateral geniculate nucleus, LGN) was included, from a larger experimental program, with three adult rhesus macaques (*Macaca mulatta*; 1 female; average weight: 10.11 kg). Experiments were conducted following a previously described opiate-based

anesthesia protocol ([Logothetis et al., 2010](#)). Animals were treated according to the guidelines of the European Parliament and Council Directive 2010/63/EU on the protection of animals used for experimental and other scientific purposes. Experimental protocols were approved by the local German authorities.

2.3.1. Image acquisition

Neuroimaging data were acquired using a vertical 7 Tesla NMR scanner (Bruker, Billerica, MA, U.S.A.) and Paravision software (version 5). fMRI data were acquired with a quadrature coil and double-shot gradient-echo planar imaging (GE-EPI; nominal voxel dimensions: $0.75 \times 0.75 \times 2.0$ mm; flip angle: 53°; TR/TE: 2000/19 ms; FOV: 96 × 96 mm; matrix size: 128 × 128; 20 axial slices). Slice volumes were acquired contiguously. During each experiment, a T2-weighted rapid acquisition with relaxation enhancement (RARE) scan was collected to image the native structural space (RARE factor: 8; voxel dimensions: $0.375 \times 0.375 \times 1.0$ mm; flip angle: 180°; TR/TE: 6500–8500/16 ms; FOV: 96 × 96 mm; matrix size: 256 × 256; 40 axial slices). Acquired data were converted offline from Bruker file format to 4D NifTI files using the Unix-based *pvconv*.

2.3.2. Stimulus

A flickering checkerboard stimulus was visually presented ([Logothetis et al., 1999](#)) during a 10 min GE-EPI scan, consisting of 300 volumes. The stimulus was presented for 4 sec preceded by an 8 sec OFF period, and followed by a longer 18 s OFF period, allowing return of the blood-oxygen-level-dependent (BOLD) signal to baseline. Two sessions per subject were collected and analyzed using two common software packages (SPM & AFNI) to validate the application of SARM for studying subcortical activity across different processing pipelines.

2.3.3. SPM-based image analysis

Functional data were realigned using SPM12 (Statistical Parametric Mapping; Wellcome Department of Imaging Neuroscience, London, UK) to obtain six rigid-body transformation parameters, and then aligned to each subject’s native anatomical (RARE) scan. Each subject’s RARE was subsequently translated to the NMT v2 space, and this linear transformation was applied to all relevant functional scans. Data were nonlinearly aligned using SPM-based DARTEL, a diffeomorphic warping algorithm ([Ashburner, 2007](#)), which relies on tissue class identification and segmentation. The resulting deformation matrix was applied to each individual’s RARE and fMRI images. The alignment was assessed using SPM visualization tools, as well as the Sørensen-Dice coefficient (SDC), or coincidence index, which equated twice the volume of intersection between the NMT-morphed individual scan ($V_{morphed}$) and the corresponding template and SARM atlas (V_{pop}), divided by the sum of both volumes ([Dice, 1945](#); [Sørensen, 1948](#); [Moirano et al., 2019](#)). Thus, with each volume being the number of voxels in a region mask, $SDC = 2^* |V_{morphed} \cap V_{pop}| / (|V_{morphed}| + |V_{pop}|)$. Two ROIs, or binarized region masks, were considered; one delineating the contour of the entire brain and a second delineating the dorsal lateral geniculate (DLG). The EPIs were smoothed (2 mm FWHM Gaussian) and the fMRI data were estimated using a General Linear Model (GLM). The regressors included the demeaned rigid-body motion correction transformation parameters, the visual stimulus presentation (B_1) and the baseline activity (B_0). The fMRI data were averaged across sessions for each subject, and significant activations were assessed with a T-contrast ($q < 0.05$, FDR-corrected).

2.3.4. AFNI-based image analysis

Using AFNI ([Cox, 1996](#)), functional data were processed by first computing the alignment of each subject’s T2 structural (RARE) scan to the NMT v2 template using the @animal_warper pipeline ([Jung et al., this issue](#)). To address the contrast (e.g., of CSF, GM and WM) profile inversion between NMT v2 and the functional localizer datasets, we used

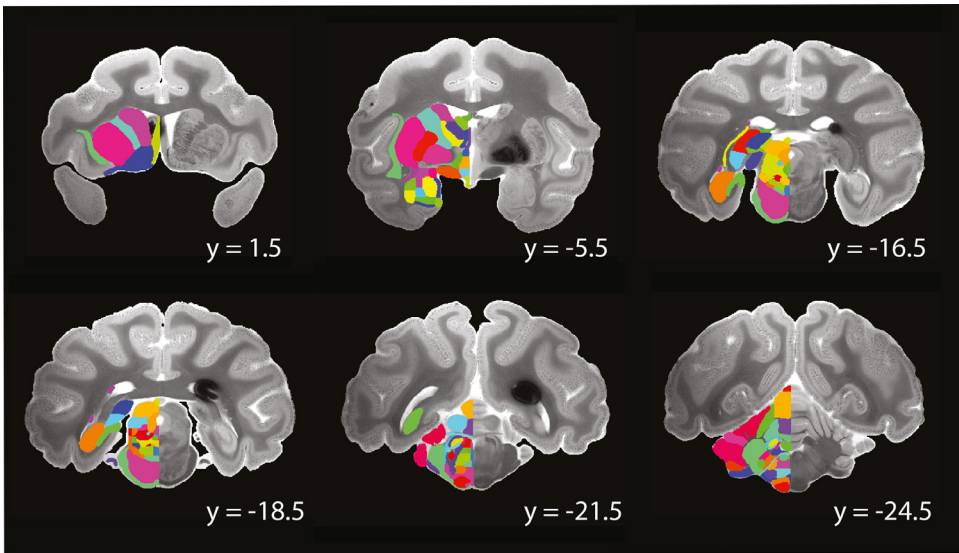


Fig. 1. The subcortical atlas in G12 space. Coronal sections from subject G12 are shown with the original subcortical parcellation overlaid for the regions in the left hemisphere. The high-resolution *ex vivo* scan was reoriented from its original orientation to a standard orientation. Coordinates are listed (in mm) in the individual subject's native space; left hemisphere shown left.

an alignment method that identifies local negative correlations to minimize the cost function, the Local Pearson Correlation (lpc; Saad, 2009). This cost function was used for both affine and nonlinear alignment. The alignment was assessed using AFNI visualization tools and the Sørensen-Dice coefficient. The affine and nonlinear transformations and the skull-stripped dataset served as the input to the functional processing performed by afni_proc.py. This processing used typical options for motion correction, alignment of the functional data to the individual's T2 anatomical dataset, and modal smoothing (by 1 voxel), followed by a per-voxel mean scaling. The normalized functional data were interpolated to an isotropic voxel of dimension 1.25 mm. The functional paradigm was modeled using a BLOCK hemodynamic response function model, stimuli convolved with a 4 sec duration boxcar function and normalized to unit size.

2.4. Data accessibility and availability

The SARM and NMT v2 files are provided in NifTI and GifTI file format for compatibility with most neuroimaging programs. This package also includes: the original G12 dataset with ROI drawings in their original space and the full list of SARM ROIs, abbreviations, and grouping levels. For data transformation and analysis, relevant scripts are also provided. All resources described are currently openly available on and will be updated through the PRIME-Resource Exchange (<https://prime-re.github.io/>, select Templates & Atlases from the Resources menu) (Messinger et al., this issue) and Zenodo (<https://zenodo.org/record/4026520#.X10> × 95P0nlw). SARM can be downloaded along with the NMT v2 from the AFNI website (https://afni.nimh.nih.gov/pub/dist/doc/html/doc/nonhuman/macaque/tempatl/atlas_sarm.html) or using the AFNI command @Install_NMT.

3. Results

3.1. Subcortical ROI segmentation and hierarchical grouping

This first version of the SARM (SARM v1) contains 210 primary subcortical ROIs (Table S1). These ROIs were first drawn on the G12 high-resolution scan (Fig. 1), and then nonlinearly aligned to the NMT v2 population-averaged symmetrical template. Most of these ROIs were anatomically identifiable in G12 and, to some extent, in NMT v2, based on local signal contrast variations. Regions likely to be relevant for neuroimaging analyses, but not readily identifiable in either scan, were delineated based on their most likely topological localization and

neighborhood relationships, using RMBSC4 as the principal reference (Paxinos et al., 2009; Paxinos et al., in preparation). Individual ROIs represent either a single homogeneous anatomical entity, as defined in RMBSC4, or a collection of smaller cytoarchitectonic entities that could not be distinguished from one another due to a lack of contrast differentiation. Beyond the definition of the manually drawn primary ROIs, we created ROIs of progressively larger size by successively aggregating primary ROIs across six hierarchical levels. These six levels can accommodate structural and functional neuroimaging datasets of various spatial resolutions and analyses at different degrees of anatomical detail. The following sections report, successively, the alignment of G12 to NMT v2 (Section 3.1.1), general observations on the hierarchical grouping of the ROIs (Section 3.1.2), and, finally, an overview of the definition of the individual ROIs and their hierarchical groups (Section 3.1.3).

3.1.1. Alignment of G12 to NMT v2

The G12 scan and its subcortical labels were resampled to match the NMT v2 resolution (0.25 mm isotropic), and the out-of-plane detail in the G12 was interpolated to match the NMT v2 resolution. Morphological differences between the *ex vivo* G12 and the *in vivo* NMT v2 (i.e., sulcal positioning, ventricle size and *ex vivo* fixation effects, as well as the presence of artifacts like air bubbles) were observed and treated. Fig. 2 portrays the G12 *ex vivo* anatomical MRI in stereotaxic space, corresponding to the NMT v2 template at 5 representative coronal sections along the anteroposterior axis, with the warped G12 result (computed using ANTs) overlaid on the edge contours of the NMT v2 template. The 3D consistency of the completed subcortical ROIs was verified by visualizing the surface of each region using AMIRA and AFNI's surface viewer SUMA (Saad et al., 2004) (Fig. 3). To construct more natural, locally consistent regions, modal smoothing, clustering and outlier detection were employed. Any residual irregularities between the subcortical parcellation and the NMT v2 borders were resolved by manual correction (see Section 2.1.4). The resulting subcortical parcellation, forming the finest hierarchical level of the SARM (level 6; see Section 3.1.2), is shown in Figures 3 and 4.

3.1.2. Multi-scale hierarchical grouping

The 210 manually-drawn primary ROIs comprise the finest level (level 6) of the SARM. Following the same principle as in the CHARM (Jung et al., this issue), these primary ROIs formed the building blocks of six hierarchically organized levels of composite ROIs. The primary ROIs were assembled into progressively larger (and, in most cases, spatially contiguous) composite ROIs from levels 5 to 1. Each ROI, or composite ROI, at a lower level (e.g., level 4) belongs to exactly one group in

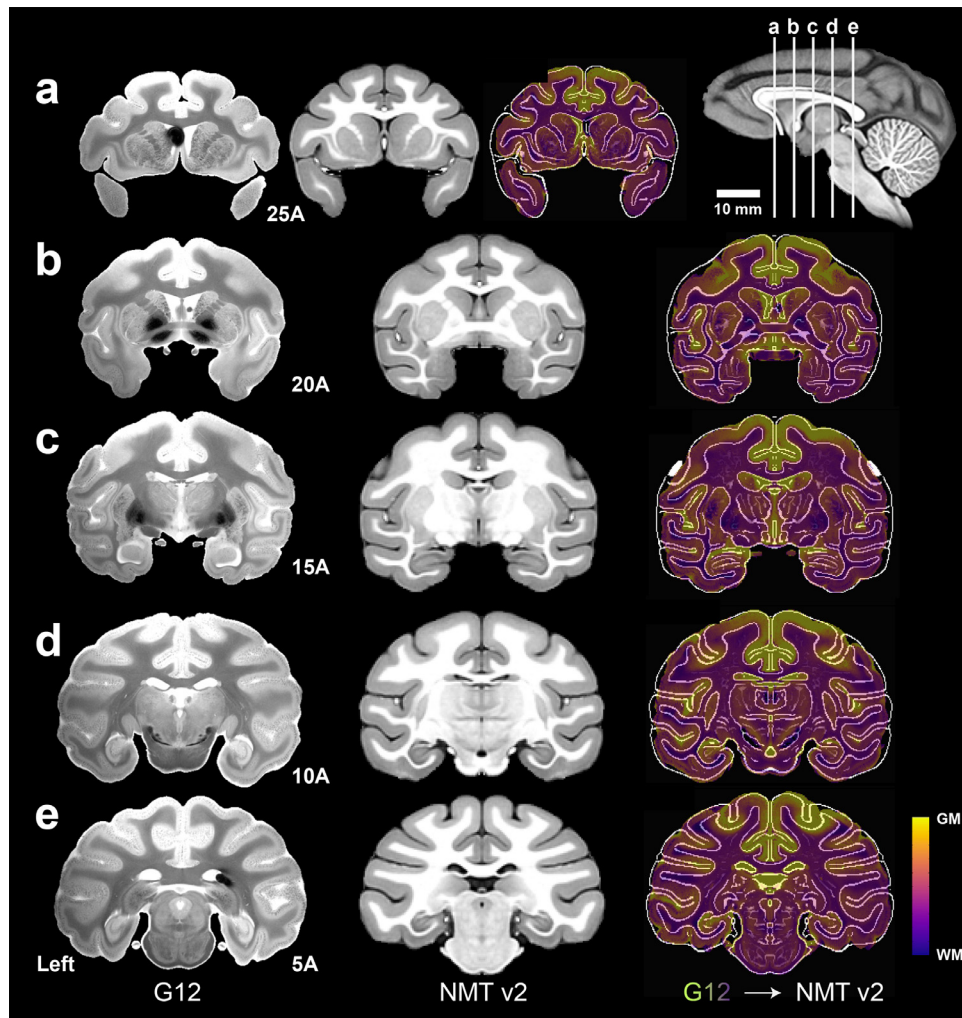


Fig. 2. Alignment of subject G12 to the symmetric NMT v2. Panels (a-e) depict coronal slices through the G12 anatomical scan (left), the symmetric NMT v2 (middle) in stereotaxic space, and the nonlinear registration of G12 (after manual treatment of air bubbles within tissue) to the symmetric template (right). Slice positions are in mm anterior to the origin (EBZ; ear bar zero) and are depicted on the mid-sagittal NMT v2 cross-section (upper right). Parameters for the ANTs registration pipeline were customized to prioritize alignment of subcortical regions. Color ('plasma') shows the warped G12 tissue intensities superimposed on the salient edges of the NMT v2. The darkest purple represents white matter (WM), whereas lighter purple and greens represent gray matter (GM). Left hemisphere depicted on the left side.

Table 2

Basic characteristics of the SARM hierarchy.

Level	# of ROIs	ROI Vol., median (mm ³)	ROI Vol., 5-95% (mm ³)
1	5	2,570.2	1,231.8 - 8,273.4
2	15	619.3	46.4 - 5,227.8
3	35	309.3	54.8 - 2,112.5
4	71	132.9	19.0 - 1,210.8
5	169	37.6	3.0 - 509.9
6	210	36.8	3.1 - 446.8

For each level of the hierarchy, the number (#) of ROIs used to parcellate the subcortex, their median bilateral volume, and the 5th-95th percentile of their volumes are listed. At lower level numbers, ROIs are combined into fewer and larger composite structures. The 5% volumes for levels 5 and 2 are smaller than for the next higher level, indicating that formation of these levels involved fusion primarily of regions larger than the 5% volumes for levels 6 and 3, respectively. Note that some ROIs exist across multiple levels of the hierarchy. The full table of SARM region names, abbreviations, and constituents is provided as a CSV spreadsheet in the distribution package and in [Table S1](#).

the next higher level (e.g., level 3). [Table 2](#) shows the number of ROIs in each level and characterizes their bilateral volumes in the NMT v2. Whole-brain coronal views of the SARM levels 2, 4, and 6 are shown in [Fig. 5](#). The various levels were designed to be suitable for either structural or functional MRI analyses, with their different spatial resolutions. Users can combine more than one grouping level within a single analysis to, for instance, examine the relationships between a specific nucleus

and larger composite brain regions. To further illustrate the SARM hierarchy, [Fig. 6](#) provides an exploration of the amygdala. The dendrogram demonstrates how the amygdala splits into its constituent regions, and these component structures are depicted on a coronal section for levels 3-6.

3.1.3. ROI and hierarchical grouping definition

Supplementary Table 1 (Table S1) itemizes the 210 ROIs at level 6 and shows their progressive hierarchical grouping, from level 5 to level 1, into a total of 325 uniquely named ROIs. Level 1 assembles all ROIs according to the classical developmental division of the neuraxis, namely the (subcortical) telencephalon, diencephalon, mesencephalon, metencephalon, and myelencephalon. The ordering of these ROIs reflects that, together, the subcortical telencephalon and diencephalon comprise the subcortical forebrain, the mesencephalon is synonymous with the midbrain, and the metencephalon and myelencephalon make up the hindbrain. Level 2 divides the telencephalon into lateral and ventral pallium (LVPal), medial pallium (MPal), amygdala (Amy), basal ganglia (BG), diagonal subpallium (DSP), and preoptic (preoptic) regions. The order in which these divisions are listed roughly follows the developmental partition proposed by [Puelles et al. \(2013\)](#), with entirely pallial groups (LVPal and MPal) first, followed by the amygdala with its pallial and subpallial components (see level 3), and, finally, by entirely subpallial groups (BG, DSP and preoptic). At level 2, the diencephalon is divided into the hypothalamus (Hy), prethalamus (PreThal), thalamus (Thal), and epithalamus (EpiThal). The mesencephalon was not divided at level 2, but the region was relabeled "midbrain" (Mid) to match the more

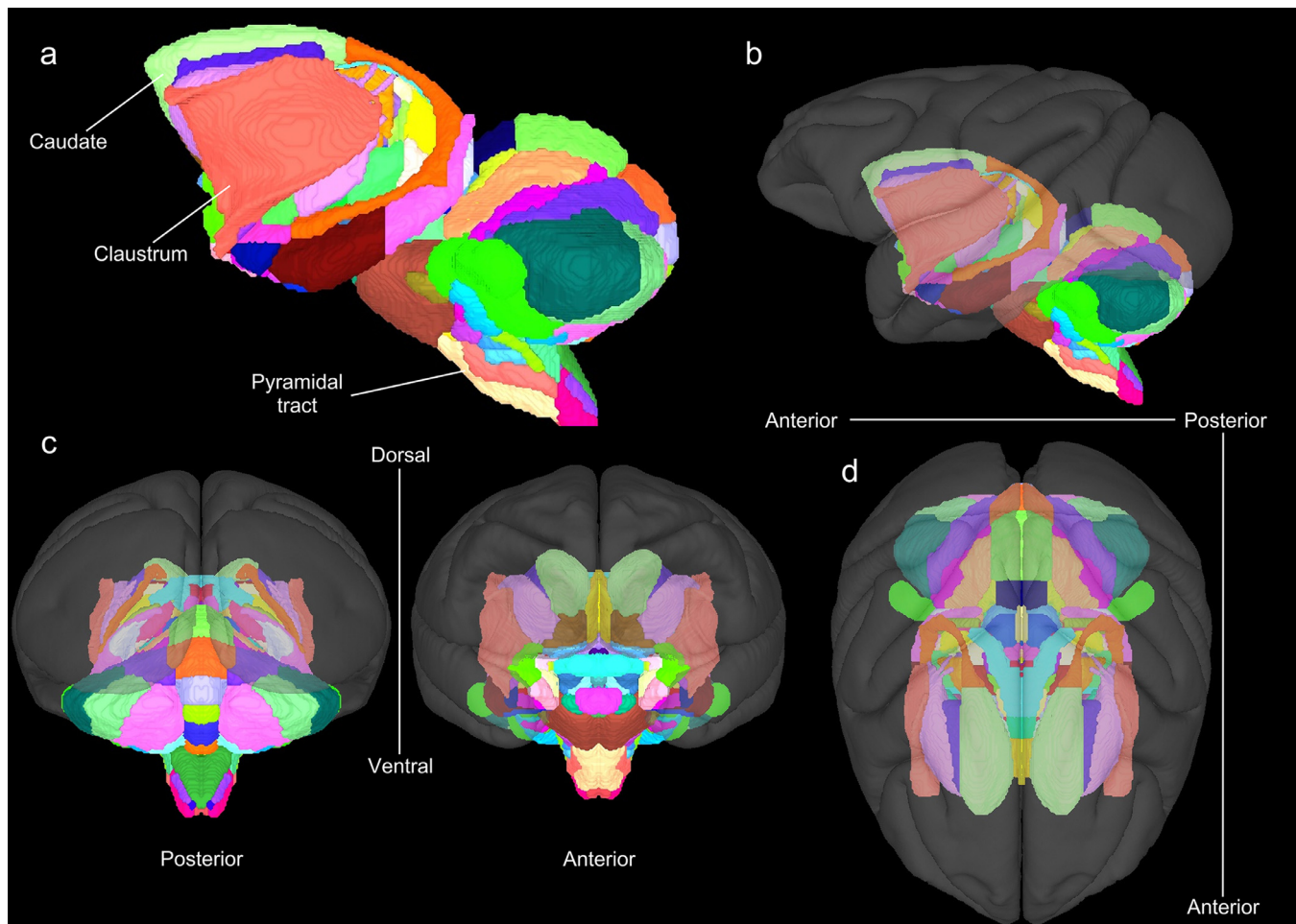


Fig. 3. Surface views of SARM (level 6) in the NMT v2.0 symmetric template. Volumetric atlas regions were converted into individual surfaces for surface-based inspection. (a) A lateral view of the subcortical surfaces, displayed in color using SUMA (Saad et al., 2004). The subcortical regions are shown with respect to the NMT v2 surface (shown in gray scale) in a (b) left lateral, (c) posterior (left), anterior (right), and (d) superior view.

common choice of terminology employed beyond level 2. Still at level 2, the metencephalon was split into the pons (Pons) and the cerebellum (Cb), whereas the myelencephalon remained whole, but switched names to the term medulla (Med). Levels 3 to 6 propose a progressively more refined parcellation of the larger groups of level 2, ending with level 6, which lists each individually drawn ROI.

Levels 5 and 6 were left largely similar to allow for future versions of the SARM to incorporate additional sub-structures. In general, beyond level 2, the hypothalamic, thalamic, mes-, met- and myel-encephalic ROIs were not grouped according to their developmental ontology (i.e., hierarchical developmental origin; Puelles et al., 2013) plan because most of the small ontologically related ROIs of these regions are spatially non-contiguous in the adult brain. Instead, these ROIs were mainly grouped according to either functional or purely topological criteria, with the practical condition that they remain contiguous, as this has greater relevance for targeting of subcortical regions and neuroimaging analytical strategies (e.g. clustering).

Table 2 provides the 5–95th percentile values of the bilateral volume of the ROIs in each level of the SARM hierarchy (see 3.1.2. Multi-Scale Hierarchical Grouping). Additionally, Supplementary Table 2 (Table S2) lists the unilateral volume in cubic millimeters of all 325 uniquely named ROIs across all 6 levels of the SARM. Of the ROIs in levels 5 and 6, only four (out of 233) are smaller than 1 mm³ and only 16 are smaller than 2 mm³. Notably, the smallest ROI (obex) is 0.125 mm³, which corresponds to eight voxels at the high resolution of the NMT v2, or one 0.5 mm isotropic voxel, and 1/27th of a typical fMRI voxel (1.5 mm

isotropic). The relevance of the small volumes to the accuracy of the drawing of the ROI boundaries in the SARM is addressed in the Discussion. The next sections briefly describe the rationale for the drawing of the ROIs and their grouping at and below level 2.

3.1.3.1. Lateral and ventral pallium. The lateral and ventral pallium (LPal) group contains 4 primary ROIs (Table S1). The claustrum (Cl) and the dorsal and ventral endopiriform claustrum (DEn and VEn) were all identifiable in the G12 (not shown) and the NMT v2 (Fig. 7a and b). DEn appeared as a separate entity at the 'heel' of Cl (see arrows in Fig. 7a). VEn was recognized by a consistently lighter contrast in comparison with the darker nuclei of the amygdala (see blue asterisk in Fig. 7a). The blood vessels (from the lenticulostriatal arteries) located at the base of the putamen (Pu) and above the 'heel' of Cl were incorporated into the Pu ROI by default (yellow asterisk in Fig. 7a). The piriform cortex (Pir; not shown) was recognized by its thinner cortical width at the medial junction of the orbitofrontal and temporal cortices (Carmichael and Price, 1994; Evrard et al., 2014), although its exact border with Cl at the limen insulae and with the amygdalo-piriform transition (APir) in the temporal lobe could not be ascertained.

At level 4, DEn and VEn are grouped in En (Table S1). At level 3, En is grouped with Pir in the ventral pallium (VPal), from which En and Pir originate along with other olfactory structures (Puelles et al., 2013) that were not segmented here (but see CHARM; Jung et al., this issue). Also at level 3, Cl constitutes the only ROI of the lateral pallium (LPal). At level 2, LPal and VPal are grouped under LVPal.

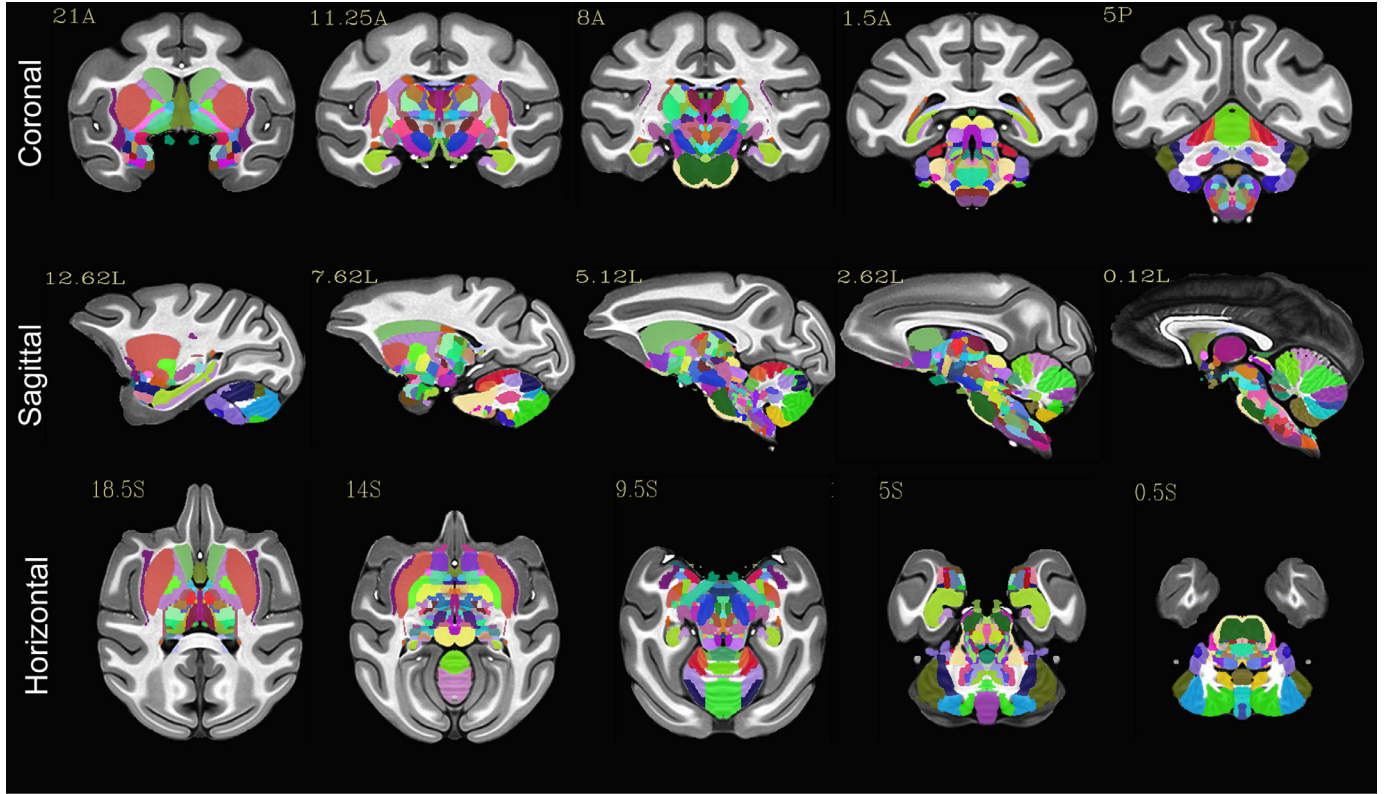


Fig. 4. Subcortical regions in NMT v2 space. The subcortical parcellation of the G12 subject was warped to the NMT v2 symmetric template and manually adjusted to match the template's morphology. These regions constitute level 6 of the SARM and are shown in color on the symmetric brain-extracted NMT v2 template. Slice coordinates relative to the origin (EBZ; ear bar zero) are in mm in the superior/inferior (top), anterior/posterior (middle), and left/right (bottom) directions.

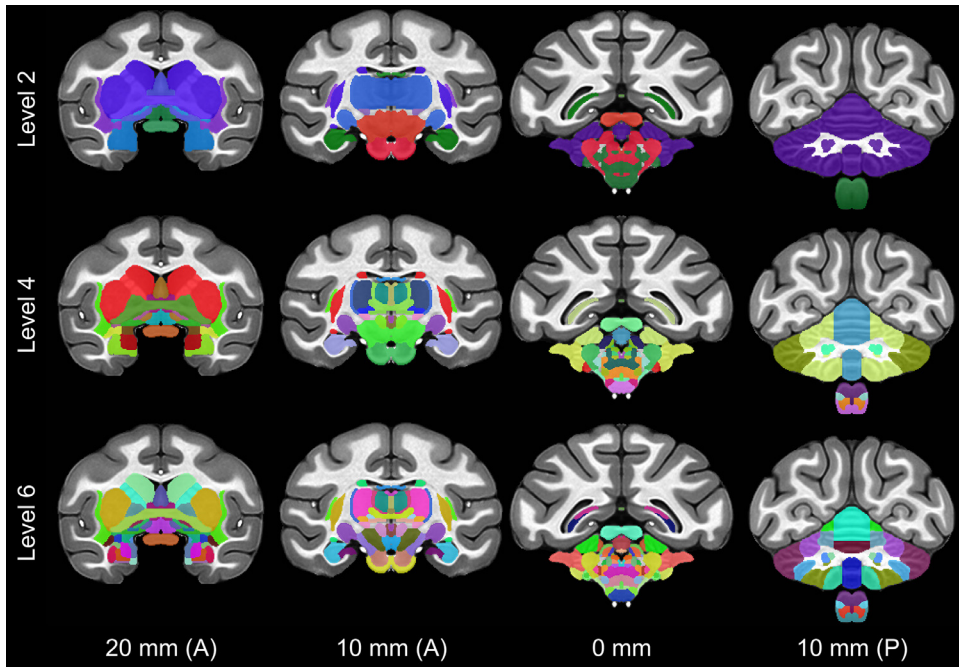
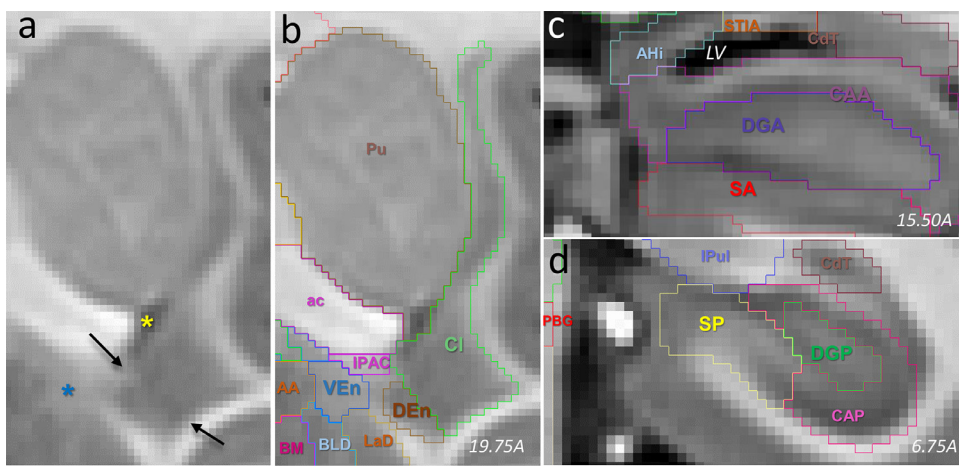
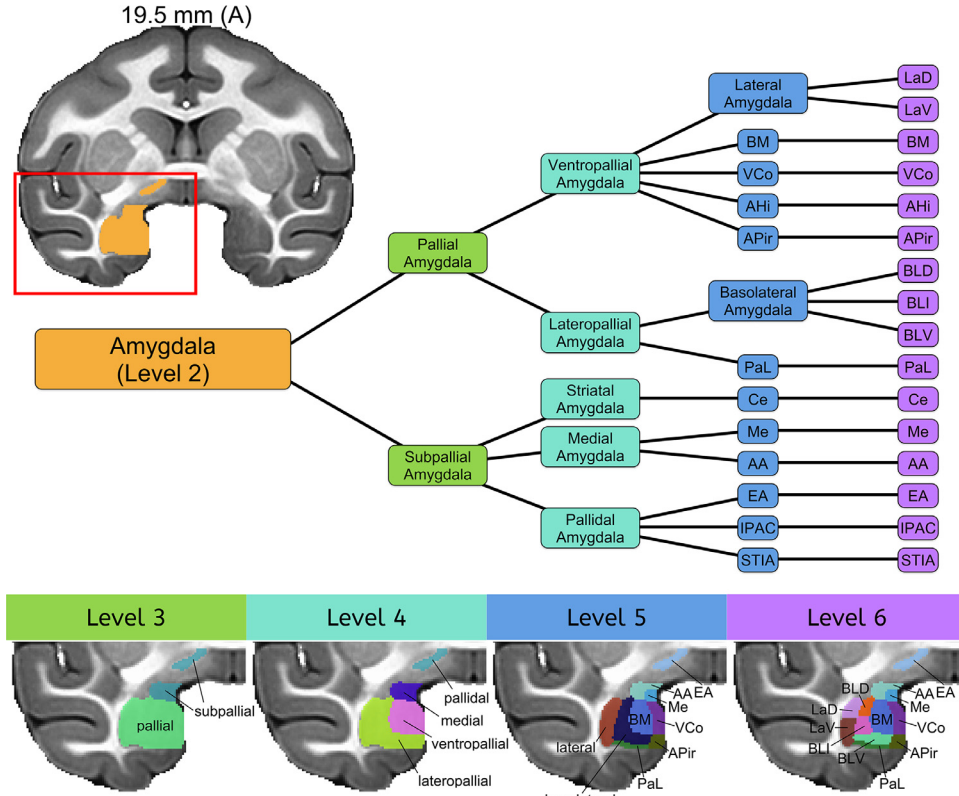


Fig. 5. SARM's Hierarchical ROI Groupings. Representative coronal slices through the symmetric NMT v2 in stereotaxic space, showing levels 2, 4 and 6 of the SARM hierarchy. Level 2 contains relatively broad composite structures, level 4 contains somewhat finer groupings, and level 6 consists of the finest anatomical segmentation. Slice coordinates are in mm anterior (A) or posterior (P) to the origin (EBZ; ear bar zero).

3.1.3.2. Medial pallium (Hippocampal Formation). The whole hippocampal formation (HF) of level 3 was divided into anterior (HFA) and posterior (HFP) halves at level 4, with a boundary placed approximately at the anteroposterior middle of the HF, taking into account evidence for a functional anteroposterior gradient in the primate HF (Strange et al., 2014). HFA and HFP were each further divided at level 5 into anterior

hippocampus (HiA) and subiculum complex (SA), and into posterior hippocampus (HiP) and subiculum complex (SP), respectively. HiA and HiP were further divided at level 6 into anterior dentate gyrus (DGA) and CA1-3 (CAA), and into posterior dentate gyrus (DGP) and CA1-3 (CAP) (Table S1; Fig. 7c and d). The distinction between the dentate gyrus (DG) and CA1-3 regions was based on a subtle change in contrast from



dark in CA1-3 to light in DG, as well as on their most plausible localization within the HF (Paxinos et al., in preparation). Although being acellular, the fimbria (fi) was grouped with HFP and HF at levels 4 and 3, respectively, in order to take into account the lower spatial resolution of functional scans that may not distinguish fi from Hi and S. The fornix (f) was drawn throughout the lateral ventricle mainly for illustrative purposes. It was not added to the HF group to avoid false attribution of activation possibly originating from regions located in the vicinity of the distant f (e.g., septum and dorsal thalamus). Finally, at level 2, HF and f were grouped together in the medial pallium (MPal), from which they originate during development (Puelles et al., 2013).

3.1.3.3. Amygdala. The amygdala was delineated into 16 primary ROIs (Table S1). Fig. 8 illustrates the segmentation of the amygdala at one representative anteroposterior level in NMT v2, G12 and RMBSC4. Throughout the anteroposterior extent of the amygdala, the dorsal and ventral parts of the lateral amygdaloid nucleus (LaD and LaV) were recognizable by their darker contrast, compared to the lighter dorsal, intermediate and ventral parts of the basolateral nucleus (BLD, BLI and BLV). The theoretical location of the basomedial nucleus (BM) often contained a darker region in both NMT v2 and G12, which likely corresponds to the parvocellular or magnocellular division of BM and contrasts with the lighter and more homogeneous ventral cortical nucleus (VCo). The

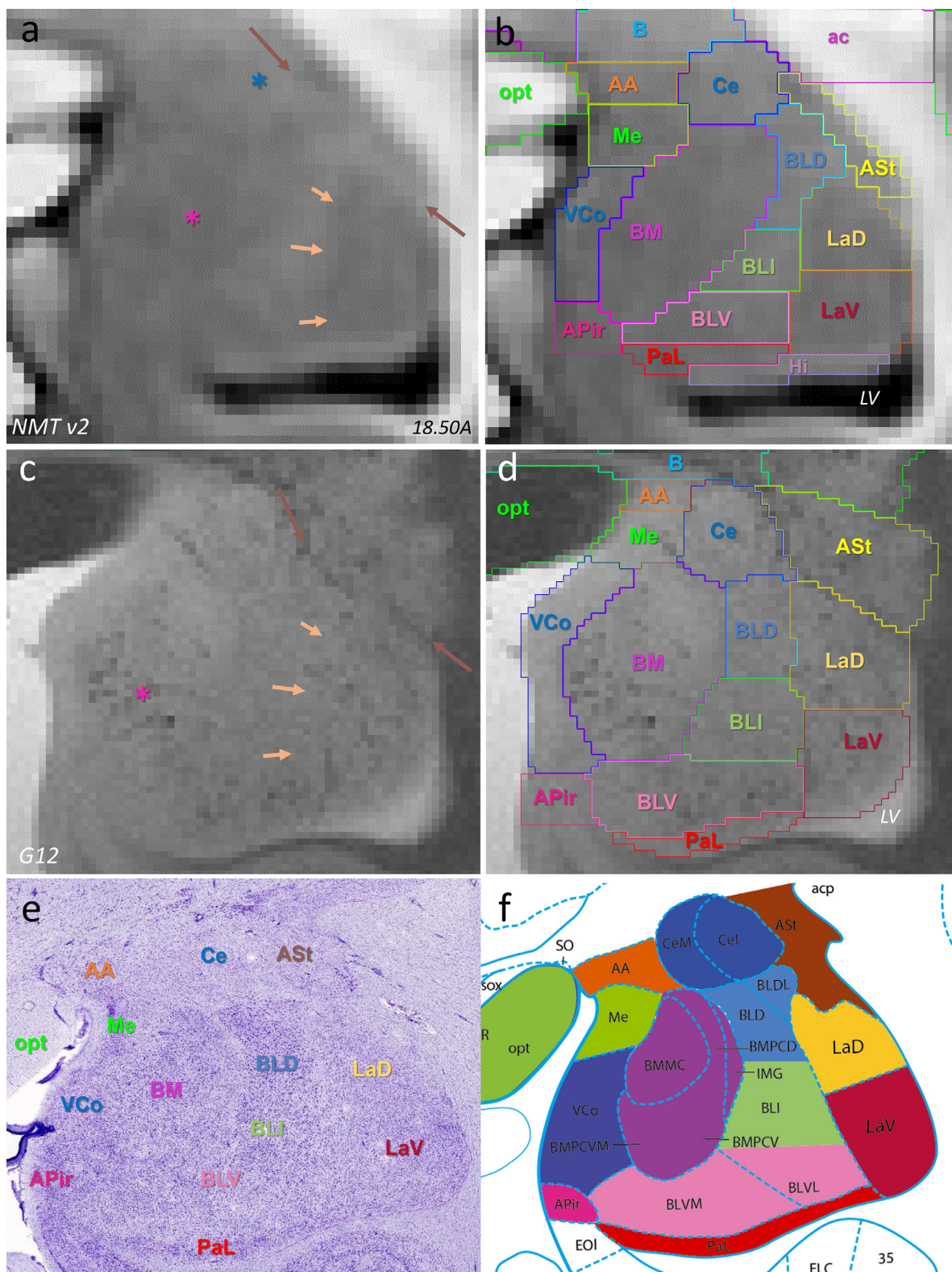


Fig. 8. SARM's amygdaloid ROIs. Coronal slices through the right hemisphere at approximately the same location in (a, b) NMT v2, (c, d) G12, and (e,f) a corresponding pair of RMBCS4 Nissl-stained section and diagram (Fig. 56). The brown arrow in (a,c) points at the boundary between ASt and the amygdala. The blue asterisk in (a) points at a zone of lighter contrast, likely corresponding to Ce. The light orange arrows in (a, c) point at the putative border of LaD and LaV with BLD, BLI and BLV. The mauve asterisks in panels (a, c) mark the darker contrast included in BM. **Abbreviations:** AA, anterior amygdaloid area; ac, anterior commissure; APir, amygdalopiriform transition area; ASt, amygdalostriatal transition area; B, basal n.; BLD, BLI, BLV, dorsal, intermediate and ventral parts of the basolateral amygdaloid n.; BM, basomedial amygdaloid n.; Ce, central amygdaloid n.; LaD and LaV, dorsal and ventral parts of the lateral amygdaloid n.; LV, lateral ventricle; Me, medial amygdaloid n.; opt, optic tract/chiasma; PaL, paralaminal amygdaloid n.; VCo, ventral cortical amygdaloid n.. In all panels, left is medial and top is dorsal.

paralaminar nucleus (PaL) appeared as a thin sheet of lighter (G12), and somewhat darker (NMT v2), contrast at the base of the amygdala. The central nucleus (Ce) was less distinct, but its theoretical anatomical location largely corresponded to a circular area with a lighter contrast in NMT v2. Medial to Ce, AA and the medial nucleus (Me) appeared darker in NMT v2 and lighter in G12. The boundaries between Me and AA, between BLD, BLI, and BLV, and between LaD and LaV were drawn based on their theoretical topological localization (Amaral et al., 1992; Stefanacci et al., 2000; Paxinos et al., 2009). Lateral to the amygdala, the amygdalostriatal transition area (AST) appears as a distinct region, separated by a thin but distinct lighter (NMT v2) or darker (G12) strip of white matter. Dorsal to the amygdala proper, the interstitial nucleus of the posterior part of the anterior commissure (IPAC), the intraamygdaloid division of the bed nucleus of the stria terminalis (STIA), and the extended amygdala (EA) are all readily distinguishable in NMT v2. For example, EA appears as a distinct lighter band underneath the ventral pallidum (VP) (Fig. 9a).

As shown in Fig. 6, the amygdala is divided at level 3 on developmental grounds into its pallial and subpallial portions. At level 4, the former splits into the portions arising from the ventral and lateral pallium, while the latter divides into the striatal, medial, and pallidal amygdala. These are then further divided into individual nuclei (level 5) and, in the case of the lateral and basolateral nuclei, into subnuclei (level 6). The different ROIs of the pallidal amygdala are not all contiguous. For example, EA has no boundary with other amygdaloid nuclei. Therefore, the pallidal amygdala ROI is one of the two SARM group ROIs containing non-contiguous ROIs. See 3.1.3.11 for the other exception in the medulla.

3.1.3.4. Basal ganglia. The basal ganglia (BG) was delineated into 12 primary ROIs (Table S1). The head of the caudate (CdH) and the putamen (Pu) were identifiable due to their prominent size and distinct boundary with the internal capsule (ic), anterior capsule (ac), corpus callosum (cc), external capsule (ec), and white matter of the cerebral cortex (Fig. 9). The ventral boundary between CdH and the anterior portion of the bed nucleus of the stria terminalis (ST) was marked by an abrupt darkening of the signal in ST (see also Section 3.1.3.5). The ventral boundaries of CdH and Pu with the accumbens nucleus (Acb; not shown) were identified by a consistent change to a more heterogeneous contrast pattern in Acb. The tail of the caudate (CdT) was distinct all along the lateral ventricle (LV) (Fig. 11) and in proximity to the amygdala, where it borders the amygdalostriatal transition area (AST; not shown). Taken together, the caudate, putamen and accumbens (i.e., the striatum) as well as part of the olfactory tubercle could also have been parcellated into dorsolateral, central and ventromedial ROIs, roughly reflecting the sensorimotor, associative and limbic gradient of the striatum, respectively (Haber and Knutson, 2010; Haber et al., 2012). In version 1 of the SARM (SARM v1), we elected to use the classical morphological parcellation as these borders are clear in structural MRI scans. The striatum is divided into dorsal and ventral parts at level 4; thus, this level can be used if greater striatal delineation is desired. Future updates to the SARM will adopt a parcellation at levels 6–5 that better reflects the functional and connectivity gradient organization of the striatum. The external (EGP; Fig. 9) and internal (IGP; not shown) globus pallidus were readily identifiable due to their slightly darker contrast, compared to the surrounding white matter. They were distinguishable from one another due to their characteristic shapes and their separation by the thin medial medullary lamina (not shown). The ventral pallidum (VP) appeared distinctly darker between ac and EA (Fig. 9).

At level 5, CdH and CdT were grouped as caudate (Cd); and EGP, IGP and their ventral ansa lenticularis tract (al; not shown) were grouped as globus pallidus (GP). At level 4, Cd, Pu, AST, and ic (which contains strands of neurons) were grouped as dorsal striatum (DStr), and Acb and Tu were grouped as ventral striatum (VStr). At level 3, DStr and VStr were grouped as striatum. GP, ac and VP were grouped as pallidum (Pd) at levels 4 and 3. The inclusion of white matter tracts (e.g.,

ac in Pd) enables using broad ROIs in fMRI analyses with rather low spatial resolution, and in which the BOLD signal would likely ‘spread’ over multiple neighboring structures, without possible distinction between smaller ROIs.

3.1.3.5. Diagonal subpellum. The developmental ontological definition of the diagonal subpellum (DSP) includes the basal nucleus of Meynert (B), the bed nucleus of the stria terminalis (ST), and different parts of the septum and diagonal band of Broca region (SDB and SFi) (Table S1) (Puelles et al., 2013). B is anatomically formed by an ill-defined group of cholinergic neurons at the base of the basal ganglia. In some slices of NMT v2, the putative location of B could correspond to a slightly darker region ventral to EA and VP (see blue asterisk in Fig. 9a, left); however, this appearance is not consistent. Thus, for the most part, the delineation of B is based on its most likely localization, underneath VP anteriorly (Fig. 9) and in between IGP, the optic tract (opt) and Pu posteriorly (not shown; see for example RMBS4 Fig. 66). To take into account this less obvious delineation, the region surrounding our delineation of B is labeled as ‘peri-basal region’ in the SARM v1 (PeB; Fig. 9), which corresponds, in RMBS4 to a rather undefined region sandwiched between B and other regions such as AA, Ce and SDB. B and PeB are grouped in the basal nucleus ‘region’ (BR) at levels 5 and 4. Anteriorly, the different parts of ST form a distinct ‘ring’ of dark signal around ac (ST; Fig. 10a and b). Posteriorly, ST mingles with various fiber tracts and appears lighter (Fig. 10a and b). The different components of the medial and lateral septum, as well as those of the diagonal band of Broca, were not readily distinguishable from one another in G12, although the medial portion of the septum appears lighter in NMT v2 and could be ascribed to the medial septum in a future version of the SARM (Fig. 9). Ventrally and posteriorly, SDB (i.e., SIB and HDB in Fig. 9c) is consistently darker than EA but lighter than PO, and sits ‘sandwiched’ between them. For the time being, these anterior and posteroventral regions are grouped in SDB. However, dorsally and posteriorly, one component of the septum that runs along the anterior portion of the lateral ventricle, namely the septimbral nucleus (SFi), was labeled as a distinct ROI (Fig. 10). SDB and SFi are grouped in the septum diagonal band region (SDBR) at level 4. BR, ST, and SDBR are grouped in DSP at levels 3 and 2.

3.1.3.6. Preoptic area and hypothalamus. The preoptic complex (POC; levels 2 and 3) and the hypothalamus (Hy; level 2) contain 3 and 17 ROIs, respectively (Table S1). At level 4, the POC bifurcates into the pre-optic region (POR) and the subjacent segments of the optic nerve and chiasma (opt), which, despite being functionally unrelated, were artificially merged because they frequently ‘fuse’ at low MRI resolutions. At levels 5 and 6, POR partitions into the different (poorly distinguishable) nuclei of the preoptic area (PO), *per se*, and the medial lamina terminalis, and its vascular organ (drawn together as LT-VOLT). LT-VOLT and opt are readily identifiable throughout G12 and NMT v2, due to their starkly distinct contrast and macroscopic location of LT-VOLT over opt or at the base of PO (Fig. 10a and b). PO is identified by its canonical location at the level of the optic chiasma and along the anterior part of the third ventricle (3V), as well as by its distinct darker contrast. The latter defines rather sharp boundaries with SDB, anteriorly, and with the anterior hypothalamic nucleus (AH), posteriorly, as indicated by the black arrows in Fig. 10b.

Most of the larger subdivisions of Hy are distinguishable due to local variations in signal intensity and/or the presence of specific white matter tracts, such as the mammillothalamic tract (mt). For example, the boundaries between AH, the ventral medial nucleus (VMH), and the arcuate nucleus (Arc) were marked by abrupt changes in contrast, similar to the boundary between PO and AH (see black arrows in Fig. 10b). The perifornical (PeF; not shown), retro-mammillary nucleus (RM) and, more particularly, mammillary nucleus are recognizable by their specific relation to the fornix (f) and mt, which are both identifiable as continuous dorsoventral tracts between the thalamus and hypothalamus (Fig. 10b). The mammillary nucleus of the hypothalamus (MM), which

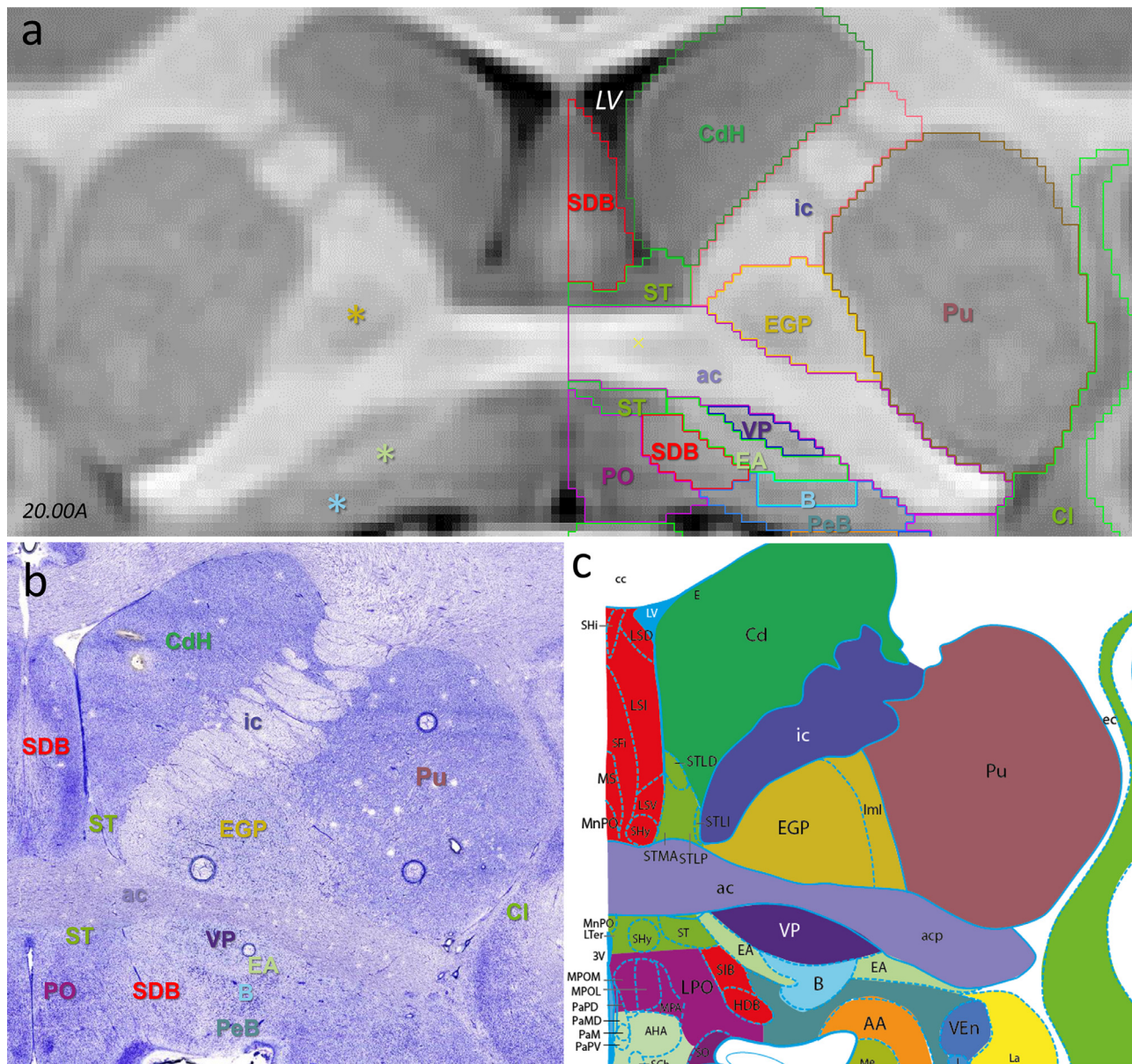
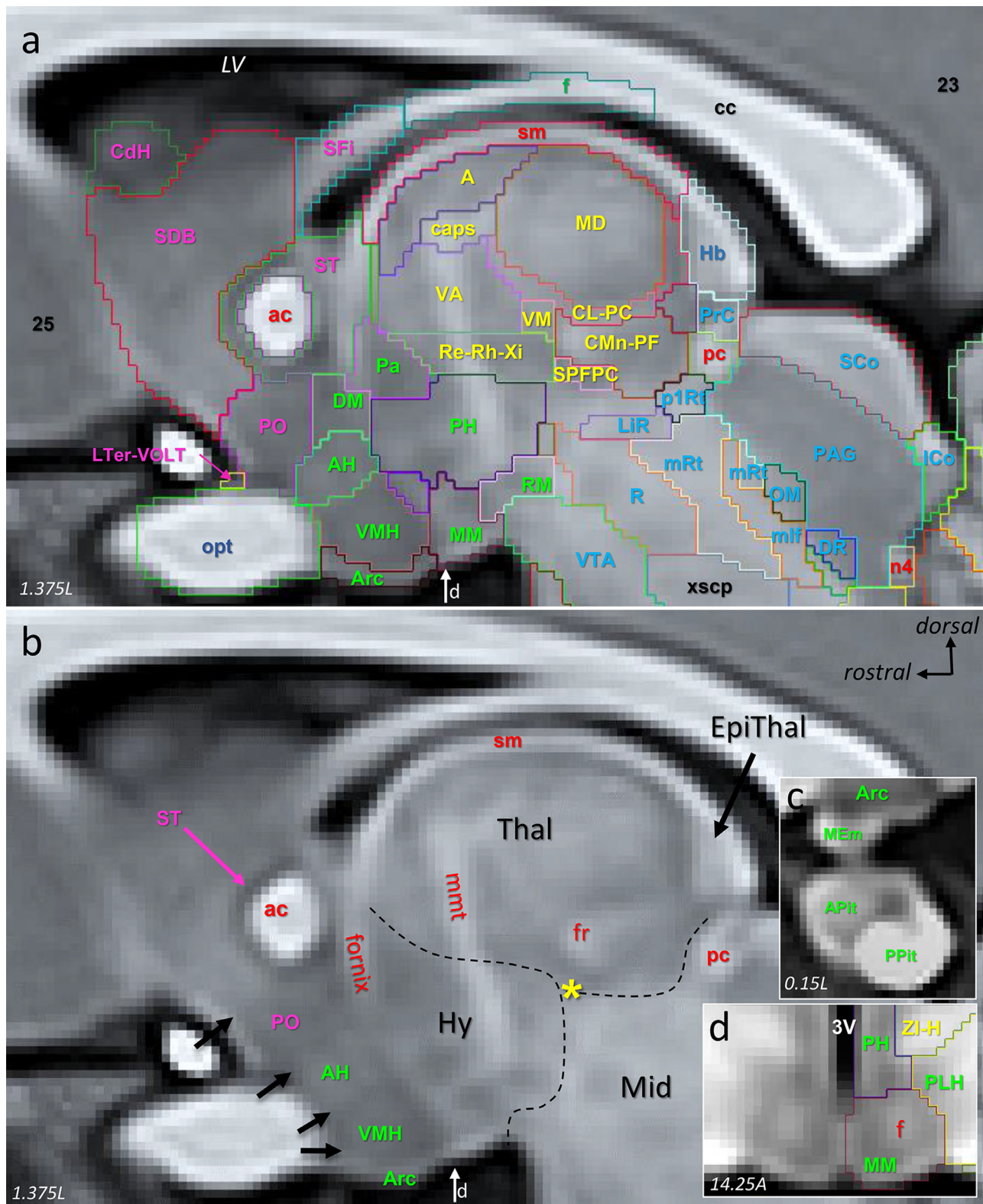


Fig. 9. SARM telencephalic ROIs. Coronal slices through (a) the symmetric NMT v2 and (b,c) the approximately corresponding pair of RMBC4 Nissl-stained section and diagram (Fig. 50). The asterisks on the left side in (a) emphasize contrasts corresponding to the location of EGP (yellow), EA (pale green), and B (blue). Only the anterior portion of SFi is included in the SDB ROI; further caudally, SFi is recognized as a single ROI (see Fig. 10a). In all panels, the top is dorsal. In (b,c), left is medial. **Abbreviations:** B, basal nucleus; CdH, head of the caudate nucleus; Cl, claustrum; EA, extended amygdala; EGP, external globus pallidus; ic, internal capsule; PeB, peri-basal region; PO, preoptic area; Pu, putamen; SDB, septum and diagonal band; SFi, septimbral n.; ST, stria terminalis; VP, ventral pallidum. For the missing abbreviations in (c), see Paxinos et al., 2009, where most abbreviations are similar to Paxinos et al., in preparation.

typically surrounds f, is also recognizable due to the bulge (mammillary body) that it forms at the base of the diencephalon (Fig. 10d). The different divisions of the lateral hypothalamic region (LHy; level 5) - that is, the lateral nucleus (LH), peduncular lateral nucleus (PLH), and juxtaparaventricular nucleus (JPLH) - are delineated mainly based on their lighter signal, compared to neighboring ROIs (not shown). The limit between the anterior LH and posterior PLH is set at the level at which the fornix reaches the hypothalamus (not shown; see RMBC4 Fig. 55). The paraventricular nucleus (Pa) and the posterior hypothalamic nucleus (PH) are distinctively darker and located medially, along 3V. The subthalamic nucleus (STh; not shown; abbreviated elsewhere as STN), which is also part of the hypothalamus (Puelles et al., 2013), is consistently identifiable due to a light circular signal located in-between the darker zona incerta (ZI-H; see Section 3.1.3.7) and substantia nigra (SN;

see Section 3.1.3.8). Finally, the pituitary (Pit; or hypophysis) is connected to Hy via the distinct medial eminence (MEm), and contains an anterior (APit; adenohypophysis) and a posterior (PPit; neurohypophysis) division, which are both recognizable in the NMT v2 due to much brighter contrast for PPit, compared to APit (Fig. 10c).

The hierarchical grouping of Hy is based mostly on a classical neuroanatomical grouping (Saper, 2012), rather than on developmental ontological grouping (Puelles et al., 2013), due to the non-contiguity of the alar and basal hypothalamic nuclei in the adult Hy. At level 3, Hy is divided into tuberal (THy), posterior (PPhy) and pituitary (Pit) groups (Table S1). The tuberal hypothalamus contains the paraventricular hypothalamus (Pa; also singled out as medial tuberal hypothalamus at level 4), as well as the supraoptic hypothalamus (SOpt), the ventromedial hypothalamic nucleus (VMH), the medial eminence (MEm) and the arcuate



nucleus (Arc), grouped together as ventral tuberal hypothalamus at level 4, and, finally, the anterior hypothalamic area (AH), the dorso-medial hypothalamic nucleus (DM), and the three distinct lateral hypothalamic nuclei (LH, JPLH, and PLH), grouped together as dorsal tuberal hypothalamus at level 4. The level 3 posterior hypothalamus contains the posterior nucleus *per se* (PH), as well as the prefrontal hypothalamus (PeF), the mammillary hypothalamus (MM) and the retro-mammillary hypothalamus (RMM) grouped together as ventral posterior hypothalamus at level 3. Pit forms a separate group at levels 3 and 4, with APit and PPit being considered separately at levels 5 and 6.

3.1.3.7. Epithalamus, thalamus, and prethalamus. The epithalamus (EpiThal; levels 2-3) contains the pineal gland (Pi; levels 4-6) and the habenula (Hb; levels 4-6). Pi forms a distinct round structure at the midline, above the superior colliculus (SCo) (not shown). Hb is located posterior and medial to the thalamus. It is recognizable in NMT v2 by its bright and heterogeneous signal (Fig. 10). The thalamus (Thal) contains 34 ROIs at level 6 (Table S1). These ROIs remain listed individually at level 5, except for the anterior thalamus (A) and the capsule of the anterior nucleus (caps) (Fig. 10a), which are then grouped to form the anterior thalamus region (AR) ROI. At levels 4 and 3, the ROIs are grouped into 12 and 6 larger groups, respectively. At level 4, most of the ROIs are grouped based on their connections (e.g., spinal, cerebellar, and palladio-nigral groups) and classical functional attributions (e.g., “non-specific” intralaminar and midline groups, and pulvinar group). The dorsal lateral geniculate (DLG; abbreviated elsewhere as LGN) and medial geniculate (MG) nuclei remain ungrouped at level 4, due to their size, anatomical distinctiveness, and functional specificity. At level 3, most of the level 4 ROIs are grouped into yet larger entities based purely on their location within Thal. MG and DLG are grouped into a geniculate ROI (GThal). The reticular thalamus (Rt) remains ungrouped until level 2 (Thal) due to its anatomical distinctiveness.

Most level 6 ROIs of the thalamus are distinguishable in G12 and NMT v2. For example, Fig. 11 illustrates the delineation and signal contrast of several distinct thalamic ROIs in one coronal slice of NMT v2. The boundary between some ROIs, such as the posterodorsal and posteroventral parts of the ventrolateral nucleus (VLV and VLPV), had to be based on their theoretical location and topological relationships. But, in most cases, there was a consistent shift in contrast at ROI borders, such as at the boundary between VLPV (darker) and the medial and lateral parts of the ventral nucleus (VPM-VPL; see black arrows in the left side of Fig. 11a). The brighter signal of the VPM-VPL ROI is consistent throughout its anteroposterior extent.

The delineations of the inter-mediodorsal nucleus (IMD), mediodorsal nucleus (MD) and centrolateral and paracentral nuclei (CL-PC) ROIs were marked by rather sharp changes in signal, from darker in IMD to much lighter in CL-PC. The brighter signal in the medial part of MD likely corresponds to its medial portion (MDM in RMBSC4), which could

be added in a future version of SARM. Dorsal to IMD, the stria medullaris tract, paraventricular and paratenial nuclei were grouped into one ROI (PT-PV-sm) due to their small individual sizes. Ventral to CL-PC, the centromedial and parafascicular complex (CMn-PF) is identifiable by its darker contrast, which reveals the typical wing-shaped form of CMn-PF, and by the passage of the fasciculus retroflexus (fr). fr is located just ventral to CMn-PF in Fig. 11a, but it can be seen crossing CMn-PF in the parasagittal view of NMT v2 in Fig. 10a and b and in the coronal view of Fig. 12a.

Ventral to CMn-PF, the posterior and basal parts of the ventromedial nucleus (VMPo-VMb) are identified together as a small, brighter region tucked between CMn-PF and the consistently darker and sharply delimited sub-parafascicular parvocellular ROI (SPFPC; see also Figs. 10a–12a). The ventroposterior inferior nucleus (VPI) ROI, which appears lighter in G12 (not shown), is delineated in the NMT v2 mainly based on its theoretical location at the lateral and ventral base of the thalamus, dorsal to the darker ROI of the zona incerta and H fields (ZI-H). ZI-H, which is the only ROI of the pre-thalamus (PreThal), is characterized by a thin strip of darker signal (see green asterisk in the left side of Fig. 11a), sandwiched at more anterior levels between two lighter strips, likely corresponding to the H1 and H2 fields of the lenticular fascicle (not present at the AP level shown in Fig. 10). The reticular thalamus ROI (Rt) is defined by a thin lighter ‘band’ (in coronal slices) covering the lateral aspect of Thal throughout its rostrocaudal extent. Finally, the pulvinar nucleus is divided into its classical anterior (APul), lateral (LPul), intermediate (IPul) and medial (MPul) subdivisions, with an additional delineation of the brachium of the superior colliculus (bsc) at levels 6 and 5. These ROIs are grouped into one ROI (Pul) at level 4 (Table S1; not illustrated). At level 3, Pul is joined by the lateral dorsal (LD) and lateral posterior (LP) nuclei to form the posterior thalamus (PThal) (Table S1).

3.1.3.8. Prepectum and midbrain. The small prepectum (PrT) and vast midbrain (Mid) contain 4 and 27 ROIs, respectively. The posterior commissure (pc) of the prepectum appears distinctly in the sagittal slice in Fig. 10a,b. The other 3 ROIs of the prepectum are delineated mainly based on their theoretical location in the vicinity of pc, with, however, a slight contrast differentiation for the precommissural nucleus (PrC, Fig. 10a and b) and, to a lesser extent, the posterior commissural nuclei (PCom-MCPC). The midbrain contains several large and distinct ROIs, including the periaqueductal gray (PAG), superior colliculus (SCo), inferior colliculus (ICO), and substantia nigra (SN), visible in Figs. 10a and 12 (PAG, SCo, and ICO). Some smaller ROIs could be delineated based on their distinctively darker or lighter contrast (e.g., interpeduncular nucleus, IP; pedunculopontine tegmentum, PTg; caudal pontine reticulum, PnC; dorsal and median Raphe, DR and MR; superior cerebellar peduncle, scp). Finally, other midbrain ROIs were drawn based on the localization of the aforementioned distinct ROIs. For example, a ventral

Fig. 10. SARM ROIs in parasagittal view. (a, b) Sagittal slice through the NMT v2 showing (a) the delineations of SARM regions and (b) major anatomical landmarks. In (a), ROI labels are color coded: telencephalic (magenta), hypothalamic (green), thalamic (yellow), epithalamic (dark blue), midbrain (light blue), and pons (black). Notable landmarks in (b) include the fr, mmt (not an ROI, inserted in figure for orientation purpose) and fornix. The yellow asterisk is placed just below the distinct darker contrast that characterizes SPFPC (see also Fig. 11). The thin dashed lines emphasize the distinctive change in contrast between Thal, Mid, and Hy. The pink arrow points at the ring of dark contrast of ST around ac. The four black arrows on the left side of (b) mark the contrast changes between PO, AH, VMH, and Arc. Panel (c) shows a mid-sagittal view of the subjacent (ventral to Arc) pituitary regions APit and PPit, as well as MEm. Panel (d) shows a symmetrical coronal view of MM with a distinctively lighter contrast in its center, corresponding to f. The vertical white arrow at the base of the hypothalamus in panels (a,b) indicates the anteroposterior level of the coronal view shown in panel (d). **Abbreviations:** 23 and 25, cortical areas 23 and 25; 3V, third ventricle; A, anterior thal. n.; ac, anterior commissure; AH, anterior hy. n.; APit, anterior pituitary; Arc., arcuate n.; caps, capsule of the anterior thalamic nucleus; cc, corpus callosum; CdH, head of the caudate nucleus; CL-PC, centrolateral and paracentral thal. n.; CMn-PF, centromedian and parafascicular thal. n.; DM, dorsomedial hy. n.; DR, dorsal Raphe; EpiThal, epithalamus; f, fornix; fr, fasciculus retroflexus; Hb, habenula; Hy, hypothalamus; ICO, inferior colliculus; LH, lateral hypothalamic area; LiR, linear Raphe; LTer-VOLT, lamina terminalis and vascular organ of the lamina terminalis; LV, lateral ventricle; MD, mediodorsal thal. n.; MEm, medial eminence; Mid, midbrain; mlf, medial longitudinal fascicle; MM, mammillary n.; mRt, midbrain reticulum; n4, 4th cranial nerve (crossing); OM, oculomotor complex; pIRT, prosomere 1 reticulum; Pa, paraventricular hy. n.; PAG, periaqueductal gray; pc, posterior commissure; PH, posterior hy. n.; PLH, peduncular lateral hypothalamus; PO, preoptic area; PPit, posterior pituitary; PrC, precommissural n.; R, red n.; Re-Rh-Xi, reunions, rhomboid and xiphoid thal. n.; RM, retro-mammillary n.; SCo, superior colliculus; SDB, septum-diagonal band; SFi, septimbral n.; sm, stria medullaris; SPFPC, subparafascicular parvocellular thal. n.; ST, bed n. of the stria terminalis; Thal, thalamus; VA, ventral anterior thal. n.; VM, ventromedial thal. n.; VMH, ventromedial hy. n.; VTA, ventral tegmental area; xscp, crossing of the superior cerebellar peduncle; ZI-H, zona incerta and lenticular fascicles (H fields).

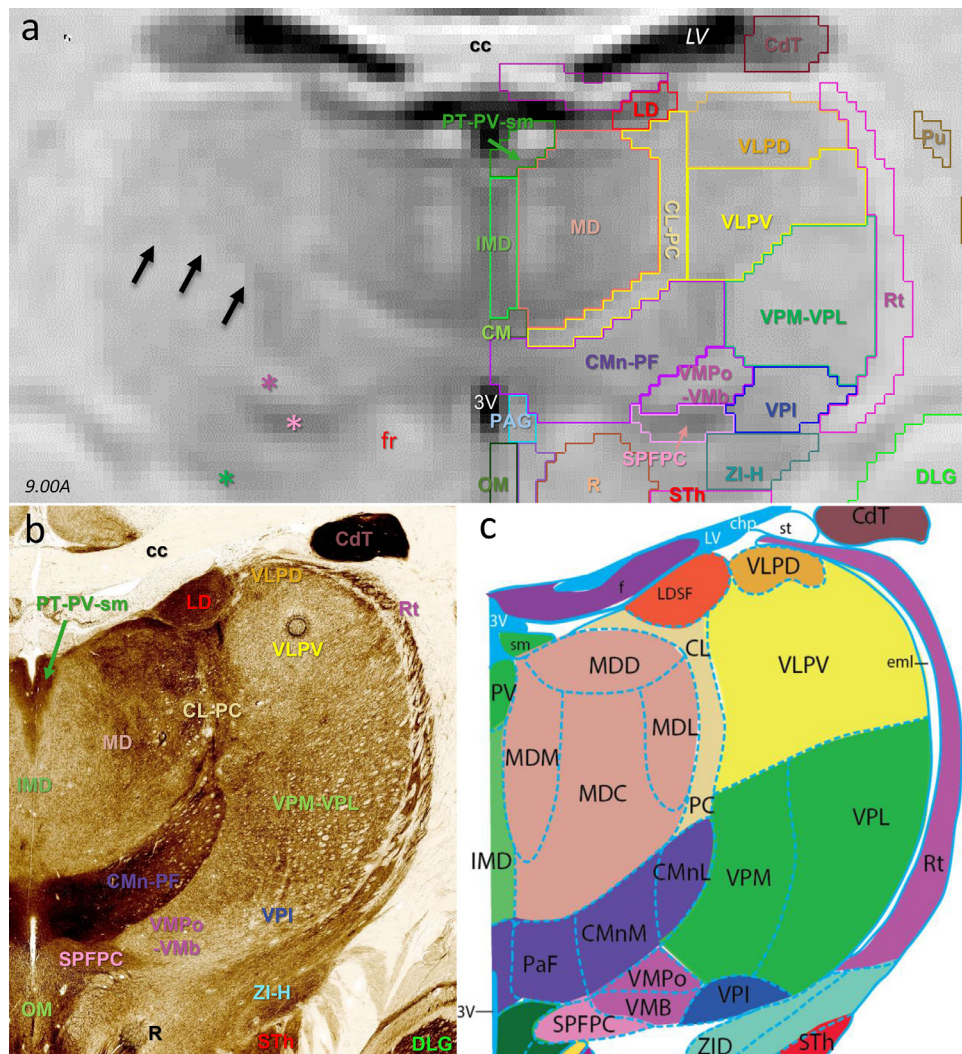


Fig. 11. SARM's thalamic ROIs in coronal view. (a-c) Coronal slice through the NMT v2 in stereotaxic space (a), and a corresponding pair of RMBS4 Nissl AChE stain section (b) and diagram (c) (Fig. 71). In (a), the black arrows point at the boundary between VLPV and VPM-VPL. The asterisks emphasize the localizations of VMPo-VMB (dark pink), SPFPC (light pink), and ZI-H (green). The red “fr” indicates the localization of the fasciculus retroflexus, ventral to CMn-PF. (In more posterior slices, fr ascends through CMn-Pf, as illustrated in Figs. 10b and 12a.) **Abbreviations (a,b):** 3v, third ventricle; CdT, the tail of the caudate; CL-PC, centrolateral and paracentral thal. n.; CM, central medial thal. n.; CMn-PF, centromedial and parafascicular thal. n.; DLG, dorsolateral geniculate thal. n.; IMD, intermediodorsal thal. n.; LD, laterodorsal thal. n.; LV, lateral ventricle; MD, mediodorsal thal. n.; OM, oculomotor complex; PAG, periaqueductal gray; R, red n.; Rt, reticular thal. n.; Pu, putamen; PT-PV-sm, ensemble of the stria medullaris, paraventral nucleus and paratenial thal. n.; SPFPC, subparafascicular parvocellular thal. n.; STh, subthalamic n.; VLPD and VLPV, posterodorsal and posteroventral parts of the ventrolateral thal. n.; VMPo-VMB, posterior and basal parts of the ventromedial thal. n.; VPI, ventroposterior medial and lateral thal. n.; Zi-H, zona incerta and lenticular fascicles (H fields). For the missing abbreviations in (c), see Paxinos et al., 2009, where most abbreviations are similar to Paxinos et al., in preparation.

tegmental ROI was drawn at the base of the midbrain, near its junction with the retro-mammillary nucleus of the hypothalamus (RM), dorsal to the distinctly darker IP, and in between the ventral halves of SN. Lastly, the red nucleus (R) was drawn based on the occurrence of a slight contrast variation forming an ovoid region, dorsal to VTA (Fig. 12a).

In the pretectum, pc and two small adjacent ROIs PrC and PCom-MCPC are grouped at level 5 as the posterior commissural region (PCR), to which the prosomeric 1 reticular formation (p1Rt) is added at levels 2–4, to form the PrT ROI. In the midbrain, most level 6 ROIs remain the same at level 5, except for the sagittum nucleus ROI (Sag-RL), which joins ICo to form the inferior colliculus complex (ICoC). At level 4, ROIs are grouped mainly based on coarse anatomical or cytological relatedness. For example, SCo and ICoC are grouped into a colliculi (Co) ROI; the several tegmental nuclei (e.g., microcellular tegmentum, MiTg, and anterior tegmental nucleus, ATg) are grouped into a midbrain tegmentum ROI (TgMid). Similarly, the midbrain dopaminergic complex (DA-Mid) was formed from the large midbrain dopaminergic cell group ROIs (i.e., VTA, SN and RF) and surrounding structures (e.g., IP). At level 3, these ROIs are further grouped, mainly based on their cardinal location (i.e., dorsal, lateral, medial, and ventral).

3.1.3.9. Pons. The ‘pons’ region of the metencephalon contains 24 ROIs (Table S1), mostly illustrated in Fig. 12. The most prominent pons ROI is the pontine nucleus (Pn), located ventrally and well demarcated from

the medial cerebellar peduncle (mcp) (Fig. 12a,c,d). The superior olive (SuO) forms a bright column posterior to Pn and directly anterior to the darker Nu7 (Fig. 12b, c and e). The lateral and medial parabrachial nuclei (LPB and MPB) form darker bands around the superior cerebellar peduncle (scp), with LPB being posterior to the lighter PTg (Fig. 12b,c,e). Lateral to MPB, we ascribed a small region to an ROI putatively containing both the locus coeruleus and the mesencephalic trigeminal nucleus (Me5). The localization of this ROI is supported by the position of the central gray nucleus (CG), recognizable medial to MPB, and the presence of a small lighter region that corresponds most likely to the efferent trigeminal mesencephalic nerve (me5; marked by the red asterisks in Fig. 12c,e). The lateral lemniscus complex (ll+), which carries projections from the cochlear nucleus, was identified as a light bundle in the lateral portion of the pons, between SuO and ICo, which both receive cochlear inputs. Within the boundaries of ll+, we drew ROIs most likely to correspond to the position of the dorsal (DLL) and inferior and ventral (ILL-VLL) lateral lemniscal nuclei (Fig. 12b). Other pons regions, such as the oral and caudal pontine reticulum (PnO and PnC, Fig. 12b-e), were drawn based on their relative position to the structures that were readily identifiable.

3.1.3.10. Cerebellum. The cerebellum (level 2) contains 27 ROIs (Table S1), including 21 cortical ROIs, 4 deep nuclei ROIs, and 2 fiber tracts. The 21 cortical areas consist of the 10 lobules, which are partitioned

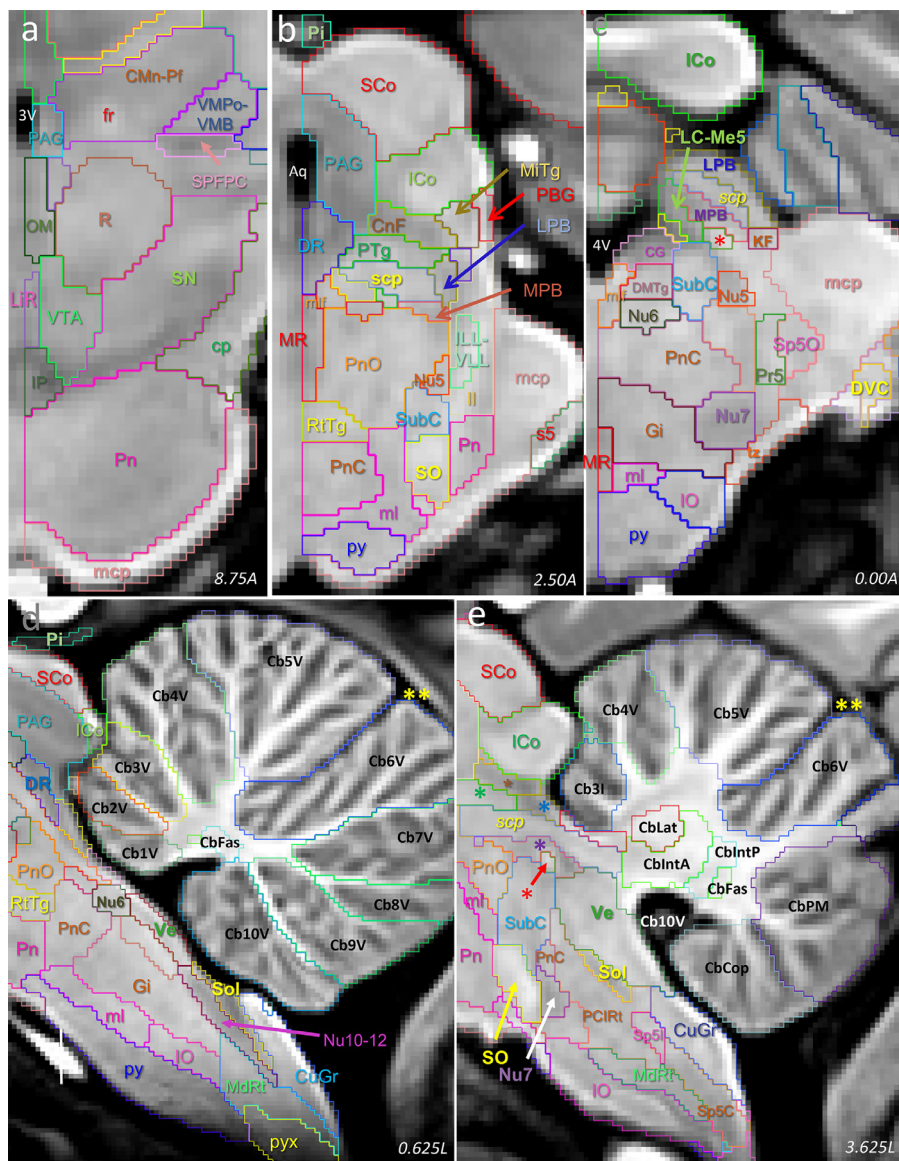


Fig. 12. SARM hindbrain ROIs in coronal and parasagittal views. Coronal (a-c) and parasagittal (d,e) slices through the NMT v2 showing ROI delineations at various levels of the neuraxis. In (d,e), the double yellow asterisks indicate the position of the anterior cerebellar fissure that separates anterior and posterior lobes. In (e), the asterisks indicate the locations of CnF (brown), PTg (green), LPB (blue), and MPB (purple). The red asterisk indicates the location of the me5. In (a-c), left is medial and top is dorsal. In (d,e) left is rostral and top is dorsal. **Abbreviations:** **3V**, third ventricle; **4V**, fourth ventricle; **Aq**, aqueduct; **Cb3I**, intermediate part of the cerebellar lobule 3; **Cb1-10V**, vermis part of cerebellar lobules 1-10; **CG**, central gray n.; **CMn-PF**, centromedial and parafascicular thal. n.; **CnF**, cuneiform n.; **CbCop**, cerebellar copula; **cp**, cerebral peduncle; **CuGr**, cuneate and gracile n.; **DMTg**, dorsomedial tegmentum; **DR**, dorsal Raphe; **DVC**, dorsal and ventral cochlear n.; **CbFas**, fastigial (medial) n.; **fr**, fasciculus retroflexus; **Gi**, gigantocellular reticular n.; **ICo**, inferior colliculus; **CbIntA**, anterior interposed n.; **CbIntP**, posterior interposed n.; **InO**, inferior olive; **KF**, Kolliker-Fuse n.; **CbLat**, lateral (dentate) n.; **LC-Me5**: locus coeruleus and mesencephalic 5 region; **LiR**, linear Raphe; **ll**, lateral lemniscus; **LPB**, lateral parabrachial n.; **mcp**, medial cerebellar peduncle; **MRt**, medullary reticular formation; **me5**, motor trigeminal root; **MTg**, microcellular tegmental n.; **ml**, medial lemniscus; **mlf**, medial longitudinal fascicle; **MPB**, medial parabrachial n.; **MR**, medial Raphe; **Nu5**, trigeminal motor n.; **Nu6**, abducens n.; **Nu7**, facial n.; **Nu10-12**, hypoglossal and motor vagus n.; **OM**, oculomotor complex; **PAG**, periaqueductal gray; **PBG**, parabigeminal n.; **PCIRt**, parvicellular and intermediate reticular n.; **Pi**, pineal gland; **CbPM**, paramedian cerebellar lobule; **Pn**, pontine n.; **PnC**, caudal pontine reticulum; **PnO**, oral pontine reticulum; **Pr5**, principal trigeminal sensory nucleus; **PTg**, pedunculopontine tegmentum; **py**, pyramidal tract; **pyx**, pyramidal tract decussation; **R**, red n.; **RTg**, reticulotegmental formation; **s5**, sensory root of the trigeminal nerve; **SCo**, superior colliculus; **scp**, superior cerebellar peduncle; **SN**, substantia nigra; **Sol**, solitary tract n.; **Sp5C**, caudal spinal trigeminal n.; **Sp5I**, intermediate spinal trigeminal n.; **Sp5O**, oral spinal trigeminal nucleus; **SPFPC**, subparafascicular parvocellular thal. n.; **SuO**, superior olive; **SubC**, subcoeruleus; **tz**, trapezoid bundle region; **Ve**, vestibular n.; **VMPo-VMB**, posterior and basal parts of the ventromedial thal. N.; **VTA**, ventral tegmental area.

into the more medial vermis lobules (CbV1 to CbV10; Fig. 12d) and four intermediate lobules (Cb3I to Cb6I; Cb3I is shown in Fig. 12e). The intermediate lobules are continuous with and lateral to the corresponding vermis lobules. The other cortical ROIs are the paramedian lobule (CbPM), simple lobule (CbSim), copula of the pyramis (CbCop), ansiform lobules crus 1 (CbCrus1) and crus 2 (CbCrus2) ROIs, as well as

the flocculus (CbFl) and paraflocculus (CbPf). See Fig. 12e for CbPM and CbCop. The deep nuclei are the classical lateral or dentate (CbLat), anterior interposed (CbIntA), posterior interposed (CbIntP), and medial or fastigial (CbFas) cerebellar nuclei (Fig. 12e). While the deep nuclei are clearly revealed by an abruptly darker contrast in G12 (not shown), they are identifiable only by a slightly lighter contrast in NMT v2. This

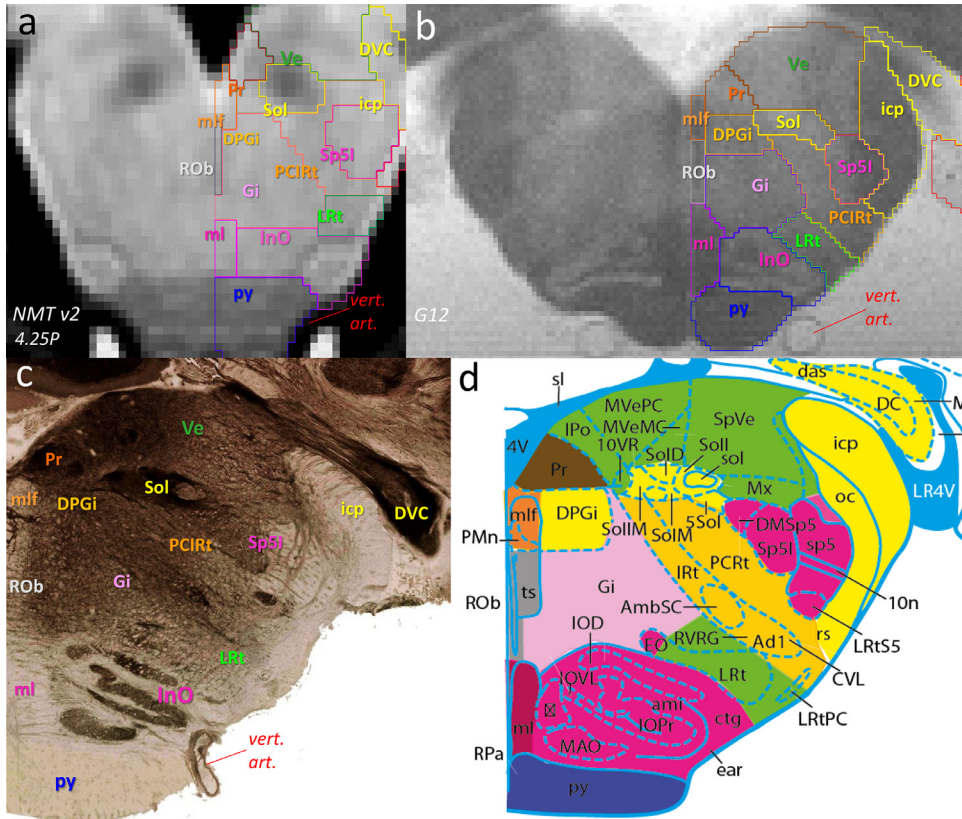


Fig. 13. SARM medullar ROIs in coronal view. Coronal slices through the left and right hemispheres of (a) the symmetrical NMT v2 and (b) G12. Corresponding RMBC4 slice through the right hemisphere showing (c) an acetylcholinesterase staining and (d) its diagram (Fig. 109). **Abbreviations:** DVC, dorsal and ventral cochlear n.; DPGi, dorsal paragigantocellular nucleus; Gi, gigantocellular reticular n.; icp, inferior cerebellar peduncle; InO, inferior olive; LRT, lateral reticular n.; ml, medial lemniscus; mlf, medial longitudinal fascicle; PCIRt, parvcellular and intermediate reticular n.; Pr, prepositus n.; py, pyramidal tract; ROb, Raphe obscurus n.; Sol, solitary tract n.; Sp5I, intermediate spinal trigeminal n.; Ve, vestibular n. In all panels, left is medial and top is dorsal. For the missing abbreviations in (d), see Paxinos et al., 2009, where most abbreviations are similar to Paxinos et al., in preparation.

slight increase in lightness is, however, sufficient to delineate the edges of each nucleus. The two tracts are the inferior cerebellar peduncle and olivocerebellar tracts, which are both located close enough to the cerebellum to be allocated to this region, instead of others (unlike mcp and scp, which are mostly represented outside the cerebellum).

At level 5, the vermis lobule ROIs are grouped into anterior and posterior vermis ROIs (AVCbCx and PVCbCx) based on the boundary defined by the primary fissure (double yellow asterisks in Fig. 12d,e) between Cb5V and Cb6V. In addition, the intermediate lobule ROIs, along with CbCop, CbSim and CbPM, are grouped into an intermediate cerebellar cortex ROI (ICbCx). Also at level 5, CbCrus 1 and 2 fuse into a lateral cerebellar cortex (LCbCx) ROI, and CbFl and CbPFI fuse into the CbFl-CbPFI ROI. At level 4, the vermis cerebellar cortex (VCbCx) ROI combines the anterior and posterior vermis ROIs, the deep cerebellar nuclei (DCb) ROI merges the deep nuclei into one, and a cerebellar ‘white matter’ (wmCb) ROI captures the two fiber tracts. At level 3, all the cortical ROIs are grouped under a cerebellar cortex ROI (CbCx), which then coexists with the DCb and wmCb ROIs.

3.1.3.11. Medulla. The myelencephalon (level 1) or medulla (level 2) contains 26 ROIs (see Table S1). Figs. 12d,e and 13 illustrate several of these ROIs. The most obvious ROIs were the solitary tract nucleus (Sol), hypoglossal and motor vagus nuclei (Nu10-12) lying directly ventral to Sol, and the facial motor nucleus (Nu7), due to their sharply delimited darker contrast. The dark Nu7 markedly contrasted against the bright contrast of SuO, which lies just anterior to Nu7 (Fig. 12e). The vestibular (Ve) and cuneate-gracile nuclei (CuGr) formed characteristic domes rostral and caudal to Sol, respectively (Fig. 12d). Ventrally, the pyramidal tract (py), decussation of the pyramidal tract (pyx), and inferior olive (InO) were identifiable by their bulging morphology and heterogeneous contrast (Figs. 12d,e; a,b). The cochlear nuclei (DVC, Fig. 13) formed a distinct structure located lateral to the medulla, within the vestibulocochlear nerve (n8). The oral, intermediate (Fig. 13), and cau-

dal spinal trigeminal nuclei (Sp5O, Sp5I, and Sp5C) form a continuous rostrocaudal column made of a medial cellular region (the nucleus itself) and of a lateral fibrous region (the nerve, sp5). Other structures, such as, for example, the paragigantocellular (Gi; Fig. 13) and medullar (MdRt) reticular nuclei, presented a rather homogeneous appearance and were drawn based on their theoretical localization, in between the identifiable regions.

At level 5, Sp5O, Sp5I, and Sp5C are grouped into a larger spinal trigeminal nucleus ROI (Sp5). At level 4, the ROIs are grouped into 8 composite structures based on their functional relatedness. For example, Ve, DVC, n8, and Pr were grouped in a larger vestibulo-cochlear complex (VCC). Among the 8 composite level 4 ROIs, the medullar Raphe (MedRaphe) and medullar motor nuclei (MedMC) are composed of non-contiguous primary ROIs. Finally, at level 3, the ROIs were grouped based on basic cardinal direction (dorsal, intermediate, and ventral medulla).

3.2. Functional localizer

3.2.1. Individual registration to SARM in NMT v2

The functional localizer data from three rhesus macaque subjects (M1-M3) were nonlinearly registered to the NMT v2 template space for analysis. The quality of the anatomical registration was visually inspected and quantified (Sections 2.3.3 and 2.3.4). As an illustration of the alignment quality, Fig. 14a-c depicts the anatomical correspondence between the three macaque subjects and the NMT v2 in the coronal and horizontal planes. A close up of the DLG in the individual scans, morphed to NMT v2 using AFNI or DARTEL, shows a favorable alignment of the individual morphed DLG with the SARM DLG for each of the three subjects, regardless of the alignment method (blue outline in Fig. 14a and b, with the possibility to compare directly with the unmarked slice showing subtle contrast changes at the boundary of DLG). The calculation of the Sørensen-Dice coefficient (SDC) for the entire brain masks

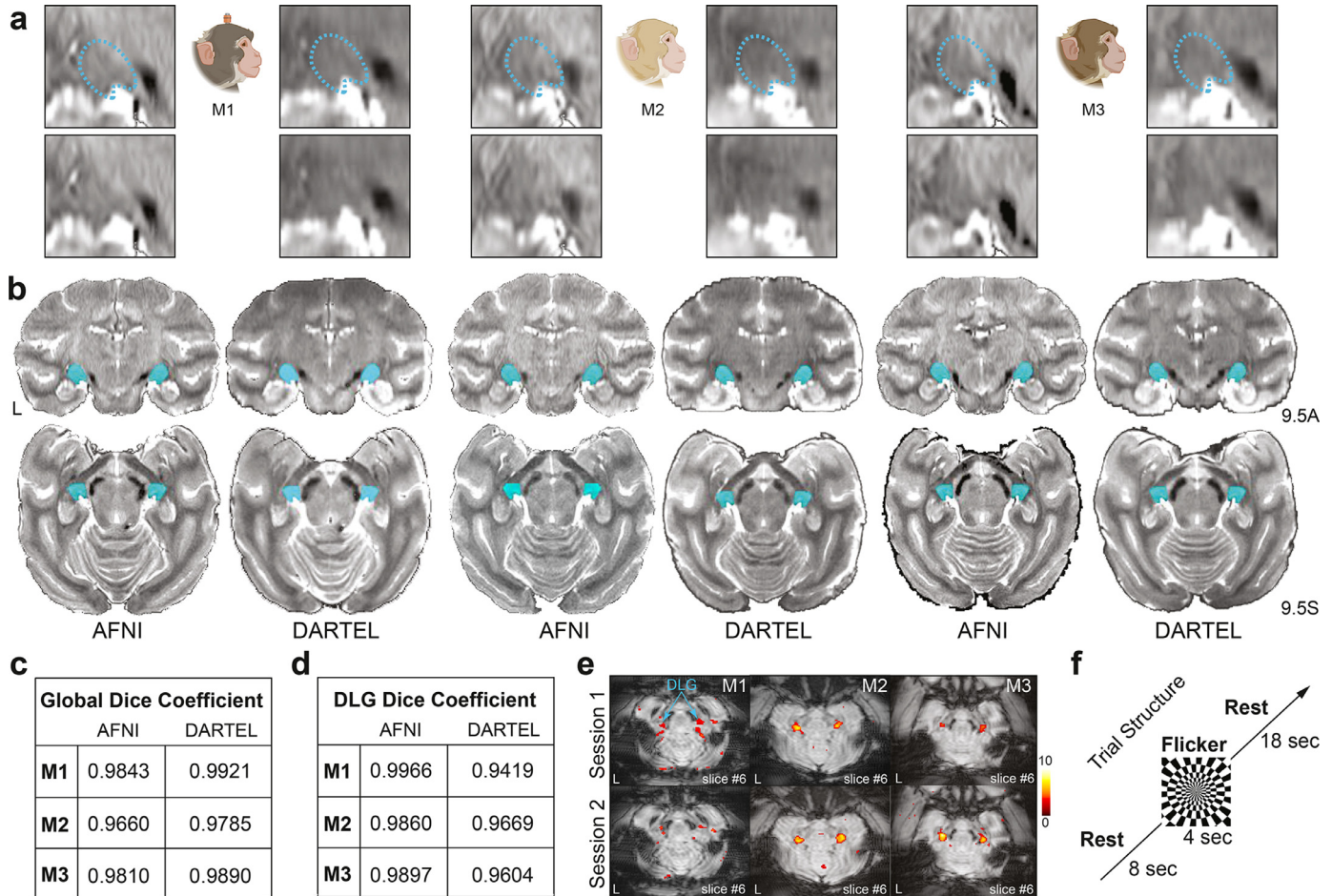


Fig. 14. Nonlinear registration of three adult rhesus macaques to the NMT v2 template. Functional localizer data was collected from two males (M1, M2) and one female (M3). Scans of M1 involved simultaneous electrophysiological recording from the brainstem. (a, b) The T2-weighted anatomical scan of each animal is shown warped to the NMT v2 population template using both the AFNI (left images) and DARTEL (right images) pipelines. DARTEL processing was conducted using SPM12. The SARM Dorsal Lateral Geniculate (DLG) ROI is overlaid in blue. (b) Alignment is shown on stereotaxic coronal (9.5A) and axial (9.5S) images (distances are in mm from the ear bar zero; EBZ). Coronal close-ups (a) show each individual's left DLG at the 9.5A level, both with (top row) and without (second row) the SARM DLG delineated in blue. The Sørensen-Dice coefficient for each subject and pipeline was computed for (c) the global positioning alignment between the nonlinearly registered single-subject scans and the NMT v2 and (d) the SARM DLG with individually refined DLG ROIs. (e) The positive BOLD response, shown in the axial plane at the dorsoventral level of the localized DLG response, correlated to the visual flicker period in the native functional scans for each of the two sessions across the cohort. (f) The temporal sequence of the functional localizer paradigm includes a rest period (no visual stimulus) preceding (8 sec) and succeeding (18 sec) each flicker presentation period (4 sec).

(morphed individual vs. NMT v2) (Fig. 14c) or for the DLG (morphed individual DLG vs. SARM DLG) (Fig. 14d) quantitatively confirmed the high quality of anatomical alignment after both AFNI and DARTEL morphing. The coefficients were close to 1 for all three subjects, with a coefficient of 1 meaning a complete overlap. For the whole brain FOV, the SDC ($\text{mean} \pm \text{STD}$) was 0.9771 ± 0.0098 and 0.9865 ± 0.0071 , for AFNI and DARTEL, respectively. For the DLG ROIs, the SDC ($\text{mean} \pm \text{STD}$) was 0.9908 ± 0.0054 and 0.9564 ± 0.0130 , for AFNI and DARTEL, respectively.

3.2.2. Subcortical activation clusters

A functional paradigm was used as a validation test to determine whether the SARM could sufficiently localize activity to an expected subcortical region. For this, we used fMRI data collected from three monkeys during a visual stimulus paradigm (flickering checkerboard; see Methods and Fig. 14f) that was shown by Logothetis and colleagues (1999) to robustly activate the DLG. All functional volumes (i.e. time points) collected were included in the analysis. From this analysis (AFNI- and SPM-based), the statistical results were computed across

2 functional scan sessions per individual. For both analysis packages, we found a consistent, bilateral responses within and in the vicinity of the DLG in native functional scans (Fig. 14e) and in NMT v2 (15a-c-d). To compare the extent of functional activity to the anatomically defined SARM atlas DLG, the significant functional activity correlated with the visual flicker stimulus in one subject (M3; Fig. 15a; $q = 0.05$, FDR-corrected) is shown in conjunction with the contour of the DLG in the NMT v2 (SARM levels 4–6; Fig. 15a and b). In the case of subject M3, almost all of the DLG was activated as determined by the fraction of functionally activated voxels in the atlas DLG (Fig. 15c). BOLD activity within this SARM region was consistently positive in all 3 macaques during presentation of the visual stimulus (Figs. 14e and 15d). (The smaller fraction of activated voxels in subject M1 may be explained by a specific preparation in this particular subject involving simultaneous physiological monitoring measurements prone to reduce BOLD signal, the description of which goes beyond the scope of the present paper. Regardless of the effect size, the activated voxels in M1 were contained in the SARM DLG.) The average BOLD percent signal change across the DLG for all subjects and hemispheres was found to

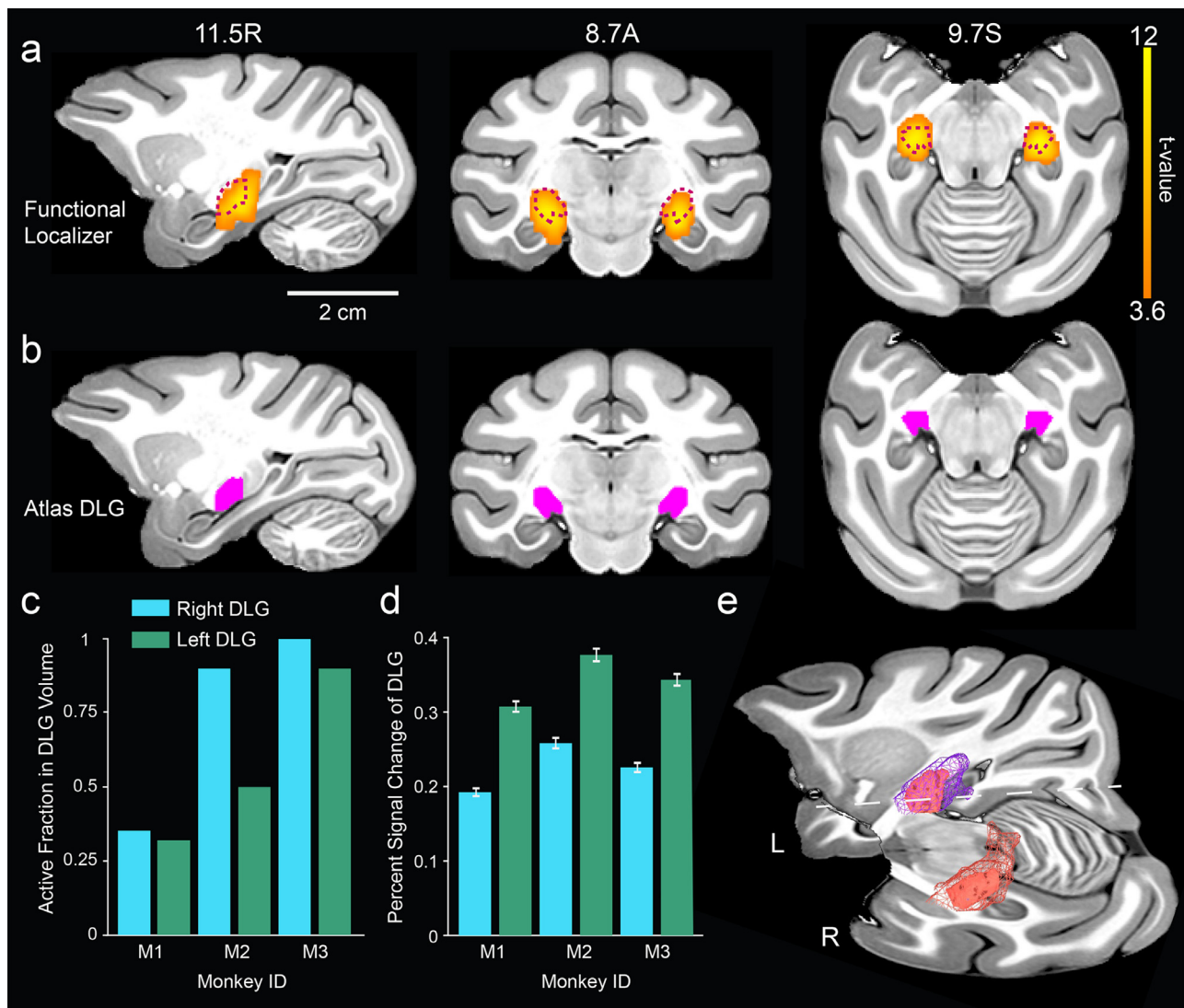


Fig. 15. Functional Localizer for DLG. The functional activity elicited in anesthetized monkeys by a flickering checkerboard stimulus was evaluated using the atlas-defined Dorsal Lateral Geniculate (DLG) region. (a) Significant positive BOLD activity elicited in monkey M3 is shown on three sections of the NMT v2 volume that include the DLG. Color shows the t-value of significantly activated voxels ($q = 0.05$, FDR-corrected; results calculated by the SPM12 analysis pipeline). The anatomical borders of the SARM's DLG are shown in (b) in magenta and with a dashed outline in (a). Slice coordinates are in mm relative to the origin (EBZ; ear bar zero). DLG activation in each hemisphere was quantified for 3 macaque monkeys (Monkey IDs: M1-M3) by (c) the fraction of functional voxels within the DLG region that were significantly activated ($q < 0.05$, FDR-corrected) and (d) the percent signal change (i.e., beta coefficient) associated with the flickering checkerboard (i.e., the 4 sec stimulus ON period) averaged across all functional voxels in the DLG. Error bars plotted represent the standard deviation. (e) 3D renderings of the DLG as defined by the atlas (smaller) and functionally by the localizer (larger) displayed in SUMA for monkey M3, against an intersecting axial and sagittal slice (unthresholded, $p < 0.07$; results calculated by the AFNI analysis pipeline).

be $0.28 \pm 0.07\%$ (mean \pm STD). To illustrate the extent of functional activation spread, a 3D rendering of subject M3's DLG-localized activation clusters with the atlas DLG (underlaid) was created using SUMA (Saad et al. 2004; Fig. 15e). Thus, based on an optimal morphing to NMT v2, this analysis shows how the SARM can be used for quantifying BOLD activity in individual ROIs and determining the specificity of functional activation.

4. Discussion

In this work, we have introduced the SARM, an MRI-based neuroanatomical parcellation atlas of the macaque monkey subcortex, designed to support the neuroanatomical localization of neuroimaging results in single-subject and group-level analyses, as well as to aid experimental subcortical targeting. The atlas is presented on the symmetric

NMT v2 population template, which reflects the average morphology of an adult rhesus macaque brain. Individual subject scans can be nonlinearly aligned to the NMT v2 for anatomical identification of activations or, conversely, the atlas can be morphed to the subject. Our own test of the SARM, using a visual stimulus as a functional localizer, confirms the accurate alignment of functional datasets to the NMT v2 and illustrates the usability of the SARM to neuroanatomically localize BOLD signal change and perform ROI-based analyses. In its present version (SARM v1), the SARM contains 210 primary ROIs at its finest spatial scale (level 6). Each ROI represents either a single cytoarchitectonic region or a collection of small neighboring cytoarchitectonic regions, based on the Rhesus Monkey Brain in Stereotaxic Coordinates atlas (Paxinos et al., 2009), with revisions that will be reflected in the new, fourth, printed edition (RMBSC4; Paxinos et al., in preparation). The iterative fusion of the finest ROIs of level 6, into progressively larger ROIs from levels

5 to 1, enables using the SARM for analyses at different spatial resolutions. Conveniently, the SARM can be used in conjunction with the Cortical Hierarchy Atlas of the Rhesus Macaque (CHARM; [Jung et al., this issue](#)), to achieve a comprehensive mapping of the macaque brain for neuroimaging.

4.1. Utility of the SARM

The SARM offers a stable neuroanatomical reference frame based on a widely used rhesus macaque brain atlas ([Paxinos et al., 2009](#); [Paxinos et al., in preparation](#)), which contributes to reducing parcellation and nomenclature discrepancies across studies, hence favoring communication on a common ground. Expectedly, due to the resolution (~0.15 mm) and contrast limits of the underlying anatomical MRI scan, the SARM does not map all minute cytoarchitectonic regions of the subcortex and, also expectedly, many small ROIs that we elected to represent could not be visualized and/or drawn with the accuracy afforded by a cytoarchitectonic atlas (see [4.3 Accuracy and Result Interpretation](#)). Thus, the SARM should not be used as an exact one-to-one neuroanatomical template, but rather as a guide supporting neuroanatomical localization and inviting the users to consider, carefully, the possible sources of functional signal in their neuroimaging datasets (e.g., fMRI, PET, and diffusion imaging). Being in stereotaxic coordinates and in NMT v2, the SARM reference frame remains fixed, regardless of changes in border definitions or the nomenclature of anatomical regions in subsequent refined versions of the SARM.

While studies using a small number of macaque subjects can be handled by directly comparing signal location to print atlases, this is a time consuming process that is subject to the judgement and training of the researcher. For greater objectivity and for studies with multiple subjects, each subject's neuroimaging data can be morphed to the common template, where the accompanying SARM atlas can be applied to conduct group-level analyses. This approach should greatly benefit studies using multiple subjects (e.g., [Logothetis et al., 2012](#); [Fox et al., 2015](#); [Grayson et al., 2017](#)), community data sharing ([Milham et al., 2018](#)), and multi-center NHP fMRI projects ([Xu et al., 2019](#)). At the structural level, the SARM can be used for deformation-based morphometry, which is commonly used in human studies (e.g., [Manera et al., 2019](#)), but has, thus far, rarely been applied in monkey studies ([Grayson et al., 2017](#)). The SARM, along with the NMT v2, can conversely be morphed to any individual's anatomical scan for volume-based morphometry. This approach enables regional voxel-based morphometric volume quantification ([Quallo et al., 2009](#)), diffusion imaging (e.g., [Zakszewski et al., 2014](#)), and functional ROI analysis ([Logothetis et al., 2012](#)) in the individual's native space before any spatial warping to fit a standard template image.

In addition to supporting data analysis, the SARM in stereotaxic space has the potential to aid with surgical planning in studies involving tracer or drug injections, lesioning, electrophysiology, optogenetics, and electrical stimulation ([Klink et al., this issue](#)). Finally, beyond studies conducted solely in macaques, provided that homology and nomenclature equivalencies can be reliably established, future harmonized versions of the SARM (subcortical), CHARM (cortical), and human atlas counterparts could further help in comparing structural and functional organization between macaques and humans at a broad scale (e.g., [Mantini et al., 2012](#)). In this context, the detail of the SARM may be especially important, for example with deep brain stimulation (DBS), where experimentally exploring spatially distinct neurostimulating sites could help explain variations in clinical results ([Ewerts et al., 2017](#)).

As with other atlases, the SARM must be used cautiously so as to avoid neuroanatomical misallocation, leading to false positives and false negatives (i.e., misattributing signal to one cytoarchitectonic region instead of its neighbor). There are two general issues that must be considered. First, users must ensure high quality alignment between their datasets and the SARM, while at the same time appreciating the notion of inter-individual variability (see [4.2 Alignment and Variability](#)). Second,

even when an optimal alignment has been reached, users must remain cautious in interpreting the allocation of signal to small ROIs, or large but heterogeneous ROIs, keeping in mind the expected and inherently acceptable constraints imposed by the MRI resolution of the SARM and the native functional scans (see [4.3 Accuracy and Result Interpretation](#)). In many cases, where the resolution or distortion of the native scans does not allow an optimal alignment, or when functional signal occurs over broad regions made of too many small ROIs or cytoarchitectonic regions, the use of the SARM's hierarchical grouping will help prevent misinterpretations (see [4.4 Multi-Scale Hierarchy](#)).

4.2. Alignment and variability

The utility of an MRI atlas is largely determined by how well data can be warped between the native individual space and the common space of the atlas. Users must carefully control the quality of their alignment, as an improper alignment will increase the risk of misinterpreting the neuroanatomical source of functional signal. Like the human brain, the exact morphology and size of the monkey brain varies across individuals. Different individuals will require more or less transformation to reach an optimal co-registration. By providing the SARM in the *in vivo* population-averaged template space of NMT v2 (rather than a single individual and/or *ex vivo* brain template), we expect that the size and morphology of most individual brains will be rather close to that of the template, facilitating the alignment. In the present study, for the task-based fMRI data, we used two distinct alignment methods, AFNI's 3dQwarp using Local Pearson Correlation (lpc; [Saad, 2009](#)) and the SPM-based diffeomorphic warping algorithm DARTEL ([Ashburner, 2007](#)). The alignment of each individual was qualitatively and quantitatively assessed (in a manner similar to [Moirano et al., 2019](#) for striatal regions). Here, the assessment focused on the subcortical DLG region ([Fig. 14a-d](#)), where the BOLD signal change was expected. Both methods produced an alignment that was visually agreeable and quantifiable via the Sørensen-Dice coefficient for the whole brain FOV (98%) and for the DLG (97%). Finally, while morphing individuals to a common template can help elucidate shared functional organization, it can also obscure inter-subject variability, reduce the chance of detecting fine local topographies (e.g., somatotopy; [Björnsdotter et al., 2009](#)), and muddle discrete inter-nuclei functional differences. In such cases, local topographies and heterogeneities can be preserved by morphing the NMT and SARM to each individual scan. The choice between morphing individual scans to the SARM and NMT, or the SARM and NMT to individual scans should be based on the questions at hand. In either case, it is highly recommended that users carefully inspect the result of their analysis in the native space of each subject ([Fig. 14e](#)) in addition to conducting group analyses.

4.3. Accuracy and result interpretation

To obtain a relatively accurate subcortical atlas, special attention was paid here to ROI positioning after alignment of the G12 parcellation to the NMT v2. We assessed this alignment visually on the structural template and examined various interpolation and regularization schemes to minimize errors. Residual inconsistencies between the subcortical labeling and the NMT v2 structure were manually corrected, ensuring a rather accurate representation of the subcortex in the NMT v2 space. However, an MRI-based digital atlas comprising ROIs representing one or several small cytoarchitectonic subcortical regions and fitted to a population-averaged template inevitably and expectedly comes with inherent approximations in terms of accuracy, of the same order of magnitude as any human atlas including similarly small ROIs. Thus, while offering obvious neuroanatomical guiding advantages, the SARM (and any atlas in fact) must be used with some skepticism in order to avoid the risk of over-interpreting functional localization beyond the capabilities of the atlas and that afforded by the resolution of functional MRI scans.

The SARM's ROIs delineate neuroanatomical regions that either clearly stand out in MRI scans (e.g., putamen or Sol) or that are less discernible, but mapped out using triangulation and in reference to their most plausible theoretical localization and size. As indicated in the Results section, Table S2 lists the unilateral volume of each of the 325 unique ROIs across all 6 levels. Users must be particularly careful when referring to small ROIs (e.g., the four ROIs $< 1 \text{ mm}^3$ through the 81 ROIs $< 10 \text{ mm}^3$, depending on the application). Some small ROIs, including even one of the smallest (mesencephalic trigeminal nerve, me5, 0.13 mm³; Fig. 12), were clearly visible in NMT v2. However, most other small ROIs were not entirely discernable (e.g., thalamic and amygdaloid sub-nuclei) or not discernable at all (e.g., LC-Me5) in the structural scans; they were instead drawn based mainly on triangulation and on their most plausible theoretical localization. While imaging resolutions will likely continue to improve, structural MRI imaging technology does not yet allow the precise visualization and localization of very small and poorly contrasted neuroanatomical regions. Thus, regardless of their visibility, the small ROIs at the finer levels of this atlas (levels 5 and 6) must be used cautiously, with structural MRI and more particularly with fMRI analyses that involve lower spatial resolution. As emphasized here, users should systematically refer to Table S2 and cautiously evaluate the pertinence of using these small ROIs. Depending on their application, lower hierarchical levels 4 or 3 may be preferable in many instances. Nevertheless, the present representation of the relative size and neighborhood relationships of the small ROIs represented at levels 5 and 6 may help users speculate on the possible origin(s) of their functional signal, and then test these origins using proper methods, such as intracerebral recording, followed with electrolytic lesion or tracer injection, and proper histological verification.

Similarly, users should also carefully consider the internal parcelation and the boundaries of larger ROIs. Some ROIs include regions that are rather functionally homogeneous (e.g., the subdivisions of ICo), while other ROIs include groups of functionally more heterogeneous regions (e.g., LC-Me5 region at level 6 or the SuO/ml ROI at level 5). Even with proper alignment, some of the latter ROIs will contain cytoarchitectonic regions with diverse connections and functions. Other larger ROIs, such as the hippocampal formation (HF), were divided into distinct sub-regions (e.g., anterior and posterior HF) based on functional and connectivity studies (e.g., Strange et al., 2014). However, in such cases, there is not always a specific structural distinction between sub-regions and the boundaries must, therefore, be taken as being an indication of a possible functional subdivision. Such subdivisions could be improved with future functional localizers (see 4.5 Future Improvements). In addition, while each ROI was drawn with painstaking care to approximate as best as possible the most plausible locations of the corresponding cytoarchitectonic region, it is to be expected that some of the ROIs will include voxels that, in fact, belong to a neighboring cytoarchitectonic region. For example, since our large ROI Ve was carefully drawn to follow the most plausible contours of the vestibular nucleus, it may slightly overlap at its edges with the adjacent principalis, solitary, and trigeminal nuclei, and vice versa. In addition, with the lower spatial voxel resolution of functional scans, and as observed in our localizer validation experiment, significant BOLD signal can spread beyond intrinsic structural landmarks. Therefore, while the SARM offers a unique neuroanatomical guide, it is strongly recommended that users examine the vicinity of functional activations and evaluate the relevance of BOLD signal overlap with specific ROIs. To this end, the whereami command in AFNI reports not only the anatomical label of the currently selected location but also that of neighboring regions in order to help identify alignment issues and other plausible sources of a functional activation.

4.4. Multi-scale hierarchy

The SARM addresses the issues of variability and accuracy by introducing hierarchical groupings at multiple spatial scales. The fine-to-gross classification scheme provides the specificity needed for use with

different resolutions. The SARM's finer levels (levels 5 and 6) may have some utility at typical functional imaging resolutions, but are especially advantageous for detailed structure analysis (e.g., MRI voxel intensity, comparisons to histological material, describing surgical, tracer or pharmacological injection sites). Level 4 of the SARM hierarchy should be rather safe for most fMRI analyses, but the higher the level, the more careful one has to be to check the quality of fMRI registration. The composite regions of levels 1-3 are sufficiently large to limit the impact of nonlinear registration errors and to ensure a sufficient number of voxels for averaging over an ROI. For example, levels 1 and 2 may be most suitable for PET studies with larger voxel sizes.

4.5. Future improvements

There are a few limitations of the current atlas implementation that could be improved in future iterations. First, while the in-plane resolution of the high-resolution scan (G12) was sufficient for definition of subcortical structures, the out-of-plane resolution (1 mm) limited the available information for tracking these structures in the anteroposterior axis. When these structures were warped to scans with higher out-of-plane resolution, manual adjustments were necessary to resolve discontinuities and inaccurate labeling driven by resampling. Such manual refinements could be minimized by scanning at high-resolution in all dimensions. Secondly, collecting a high-resolution *in vivo* scan of the G12 subject would have helped to account for disparities between *in vivo* and *ex vivo* preparations and could have acted as an intermediate target when warping between the high-resolution *ex vivo* scan and the *in vivo* NMT v2. Thirdly, *in vivo* and *ex vivo* multimodal neuroimaging would be helpful in delineating fine boundaries of subcortical structures and improve alignment to scans with differing contrast. It may also permit detecting structures that were not readily identifiable here (e.g., Ce). Lastly, subcortical atlas regions could be further delineated using connectivity-based clustering, region-specific contrasts (e.g., LC's neuromelanin; Langley et al., 2017), chemo-architectonically specific radiolabeled ligands (e.g., Oler et al., 2012; Rapan et al., 2021), and/or functional localizers (e.g., mechanoreceptive stimuli for localizing activity in thalamic nuclei CuGR and VPL-VPM or auditory stimuli to activate DVC and MG).

Another consideration unique to NHP imaging is the orientation of the brain in the scanner. Humans are typically scanned in the supine position. However, macaques are scanned in various positions, including the "sphinx" and vertical "seated" positions. These two positions change the brainstem's orientation with respect to the rest of the brain. Affine alignment is unable to correct for such relative differences, and depending on the algorithm, even nonlinear alignment tools may be limited, insofar as the brainstem can be adjusted. Further investigation is required to evaluate how well brainstem structures are registered between a stereotaxic template and functional data collected in the vertical seated orientation. Additionally, it is worth noting that *ex vivo* histological tissue sections may differ from brain imaging due to differences in features (i.e., brainstem orientation, CSF volume, ventricle size, and sulcal position). In particular, coronal sectioning through the brainstem for histological analysis is, in fact, often perpendicular to the rostrocaudal axis of the brainstem, whereas for an MR scan, coronal sections are generally oriented with respect to the telencephalon and, therefore, oblique through the rostrocaudal axis of the brainstem.

The SARM itself was conceived and developed within the context of the PRIMatE-Data and Resource Exchange (PRIME-DRE) and will greatly benefit from usage-based feedback from the community. Updates to the SARM will be released periodically based on this feedback and community forums (<https://prime-re.github.io/community>; Messinger et al., this issue). Suggestions and comments for improvement of the SARM can be emailed to the authors. We expect the atlas to be an evolving resource that will include updates based on new higher-resolution multimodal scans (structural and functional) and community-based suggestions leading to refined ROI delineations and alternative groupings,

amongst other possible optimizations and changes. Finally, while the SARM and CHARM are for the time being separate, efforts are currently underway to fuse both atlases into a single brain atlas of the rhesus macaque, with separate ROIs for the left and right hemispheres.

5. Conclusion

We have presented a new subcortical atlas for the rhesus macaque: the Subcortical Atlas of the Rhesus Macaque (SARM). Based primarily on the high-resolution MRI of a single subject and comparison with histological materials, this atlas provides the most detailed subcortical parcellation to date and is the first specifically applied to the subcortex available in a digital format for use by the MRI and general neuroscience community. We provide a specific use case and working examples of the use of this atlas within two popular fMRI analysis software packages. The SARM is part of a larger initiative in the NHP neuroimaging community to share data and resources. Information on the SARM and other macaque resources may be found at the PRIME-RE (Messinger et al., this issue).

CRediT author statement

Renée Hartig: conceptualization; resources; methodology; software; formal analysis; visualization; writing - original draft; writing - reviewing & editing

Daniel Glen: resources; methodology; software; formal analysis; visualization; data curation; writing - original draft; writing - reviewing & editing

Benjamin Jung: resources; methodology; software; formal analysis; visualization; writing - original draft; writing - reviewing & editing

Nikos K. Logothetis: resources; methodology; funding acquisition.

George Paxinos: resources; methodology; writing - reviewing & editing

Eduardo Garza-Villarreal: resources; methodology; visualization; software; formal analysis; writing - original draft; writing - reviewing & editing

Adam Messinger: conceptualization; resources; methodology; software; visualization; writing - original draft; writing - reviewing & editing

Henry C. Evrard: conceptualization; resources; methodology; visualization; writing - original draft; writing - reviewing & editing

Declaration of Competing Interest

The authors report no competing interest.

Acknowledgments

EAGV would like to thank Gabriel A. Devenyi for his feedback and support, as well as Luis A. Aguilar from the Laboratorio Nacional de Visualización Científica Avanzada (LAVIS) for the use of their computer cluster and the Laboratorio Nacional de Imagenología por Resonancia Magnética (LANIREM). RH and HCE would like to thank Michael Beyerlein and Thomas Steudel for their technical assistance with 7T imaging, Yusuke Murayama for discussions on the visual flicker paradigm, and Tatianna Saleh for her technical assistance during the final revision process. This work was funded in part by the Max Planck Society and by the Intramural Research Program of the NIMH and NINDS (ZIA MH002918 and ZICMH002888).

Supplementary materials

Supplementary material associated with this article can be found, in the online version, at doi:10.1016/j.neuroimage.2021.117996.

References

- Accolla, E.A., Dukart, J., Helms, G., Weiskopf, N., Kherif, F., Lutti, A., ... , Draganski, B., 2014. Brain tissue properties differentiate between motor and limbic basal ganglia circuits. *Hum. Brain Mapp.* 35, 5083–5092. doi:10.1002/hbm.22533.
- Amaral, D.G., Price, J.L., Pitkänen, A., Carmichael, S.T., 1992. Anatomical organization of the primate amygdaloid complex. In: Aggleton, JP (Ed.), *The Amygdala: Neurobiological Aspects of Emotion, Memory, and Mental Dysfunction*. Wiley-Liss, New York, NY, pp. 1–66.
- Arsenault, J.T., Vanduffel, W., 2019. Ventral midbrain stimulation induces perceptual learning and cortical plasticity in primates. *Nat. Commun.* 10, 3591. doi:10.1038/s41467-019-11527-9.
- Ashburner, J., 2007. A fast diffeomorphic image registration algorithm. *NeuroImage* 38, 95–113.
- Avants, B.B., Tustison, N.J., Stauffer, M., Song, G., Wu, B., Gee, J.C., 2014. The insight toolkit image registration framework. *Front. Neuroinform.* 8, 44. doi:10.3389/fninf.2014.00044.
- Baker, J.T., Patel, G.H., Corbetta, M., Snyder, L.H., 2006. Distribution of activity across the monkey cerebral cortical surface, thalamus and midbrain during rapid, visually guided saccades. *Cereb. Cortex* 16 (4), 447–459. doi:10.1093/cercor/bhi124.
- Bakker, R., Tiesinga, P., Köller, R., 2015. The Scalable Brain Atlas: instant web-based access to public brain atlases and related content. *Neuroinformatics* 13, 353–366. doi:10.1007/s12021-014-9258-x.
- Björnsdotter, M., Loken, L., Olausson, H., Vallbo, A., Wessberg, J., 2009. Somatotopic organization of gentle touch processing in the posterior insular cortex. *J. Neurosci.* 29, 9314–9320.
- Calabrese, E., Badea, A., Coe, C.L., Lubach, G.R., Shi, Y., Styner, M.A., Johnson, G.A., 2015. A diffusion tensor MRI atlas of the postmortem rhesus macaque brain. *NeuroImage* 117, 408–416.
- Calzavara, R., Zappala, A., Rozzi, S., Matelli, M., Lupino, G., 2005. Neurochemical characterization of the cerebellar-recipient motor thalamic territory in the macaque monkey. *Eur. J. Neurosci.* 21 (7), 1869–1894. doi:10.1111/j.1460-9568.2005.04020.x.
- Carmichael, S.T., Price, J.L., 1994. Architectonic subdivision of the orbital and medial prefrontal cortex in the macaque monkey. *J. Comp. Neurol.* 346 (3), 366–402.
- Cox, R.W., 1996. AFNI: software for analysis and visualization of functional magnetic resonance neuroimages. *Comput. Biomed. Res.* 29, 162–173.
- Damasio, H., 2005. *Human Brain Anatomy in Computerized Images*. Oxford University Press.
- Dice, L.R., 1945. Measures of the amount of ecological association between species. *Ecology* 26, 297–302. doi:10.2307/1932409.
- Ding, S.L., Royall, J.J., Sunkin, S.M., Ng, L., Facer, B.A.C., Lesnar, P., ... , Lein, E.S., 2016. Comprehensive cellular-resolution atlas of the adult human brain. *J. Comp. Neurol.* 524 (16), 3127–3481. doi:10.1002/cne.24080.
- Evrard, H.C., Logothetis, N.K., Craig, A.D., 2014. Modular architectonic organization of the insula in the macaque monkey. *J. Comp. Neurol.* 522 (1), 64–97.
- Evrard, H.C., Forro, T., Logothetis, N.K., 2012. Von Economo neurons in the anterior insula of the macaque monkey. *Neuron* 74 (3), 482–489. doi:10.1016/j.neuron.2012.03.003.
- Evrard, H.C., Craig, A.D., 2008. Retrograde analysis of the cerebellar projections to the posteroverentral part of the ventral lateral thalamic nucleus in the macaque monkey. *J. Comp. Neurol.* 508 (2), 286–314.
- Ewert, S., Plettig, P., Li, N., Chakravarty, M.M., Collins, D.L., Herrington, T.M., Kuehn, A.A., Horn, A., 2017. Toward defining deep brain stimulation targets in MNI space: a subcortical atlas based on multimodal MRI, histology and structural connectivity. *NeuroImage* 170, 271–282. doi:10.1016/j.neuroimage.2017.05.015.
- Felleman, D.J., Van Essen, D.C., 1991. Distributed hierarchical processing in the primate cerebral cortex. *Cereb. Cortex* 1, 1–47.
- Feng, L., Jeon, T., Yu, Q., Ouyang, M., Peng, Q., Mishra, V., Pletikos, M., Sestan, N., Miller, M.I., Mori, S., Hsiao, S., Liu, S., Huang, H., 2017. Population-averaged macaque brain atlas with high-resolution ex vivo DTI integrated into in vivo space. *Brain Struct. Funct.* 222 (9), 4131–4147. doi:10.1007/s00429-017-1463-6.
- Haber, S.N., Adler, A., Bergman, H., 2012. The basal ganglia. In: Mai, J.K., Paxinos, G. (Eds.), *The Human Nervous System*, third ed.. Academic Press.
- Haber, S.N., Knutson, B., 2010. The reward circuit: linking primate anatomy and human imaging. *Neuropsychopharmacology* 35 (1), 4–26. doi:10.1038/npp.2009.129.
- Fox, A., Oler, J.A., Shackman, A.J., Shelton, S.E., Raveendran, M., McKay, D.R., Converse, A.K., Alexander, A., Davidson, R.J., Blangero, J., Rogers, J., Kalin, N.H., 2015. Intergenerational neural mediators of early-life anxious temperament. *Proc. Natl Acad. Sci.* 112 (29), 9118–9122. doi:10.1073/pnas.1508593112.
- Hilgetag, C.C., Goulas, A., 2020. ‘Hierarchy’ in the organization of brain networks. *Philos. Trans. R. Soc. B* 375, 20190319. doi:10.1098/rstb.2019.0319.
- Grayson, D.S., Bliss-Moreau, E., Bennett, J., Lavenex, P., Amaral, D.G., 2017. Neural reorganization due to neonatal amygdala lesions in the rhesus monkey: changes in morphology and network structure. *Cereb. Cortex* 27, 3240–3253.
- Horsley, V., Clarke, R.H., 1908. The structure and functions of the cerebellum examined by a new method. *Brain* 31 (1), 45–124. doi:10.1093/brain/31.1.45.
- Jung, B., Taylor, P.A., Seiditz, J., Sponheim, C., Perkins, P., Ungerleider, L.G., Glen, D., Messinger, A., 2020. A comprehensive macaque fMRI pipeline and hierarchical atlas. *NeuroImage*.
- Klink, P.C., Aubry, J.-F., Ferrera, V., Fox, A., Froudast-Walsh, S., Jarraya, B., Konofagou, E., Krauzlis, R., Messinger, A., Mitchell, A.S., Ortiz-Rios, M., Oya, H., Premereur, E., Roberts, A., Roe, A., Rushworth, M.F.S., Sallet, J., Schmid, M.C., Schroeder, C.E., Tassière, J., Tsao, D., Uhrig, L., Vanduffel, W., Wilke, M., Kagan, I., Petkov, C.I. Combined Brain Perturbation and Neuroimaging in Non-human Primates. *NeuroImage*. This issue. doi:10.1016/j.neuroimage.2021.118017

- Kochunov, P., Lancaster, J.L., Thompson, P., Woods, R., Mazziotta, J., Hardies, J., Fox, P., 2001. Regional spatial normalization: toward an optimal target. *J. Comput. Assist. Tomogr.* 25 (5), 805–816.
- Koelle, G.B., Friedenwald, J.A., 1949. A histochemical method for localizing choline esterase activity. *Proc. Soc. Exp. Biol. Med.* 70 (4), 617–622.
- Langley, J., Huddleston, D.E., Liu, C.J., Hu, X., 2017. Reproducibility of locus coeruleus and substantia nigra imaging with neuromelanin sensitive MRI. *MAGMA* 30 (2), 121–125.
- Lewis, P.R., 1961. The effect of varying the conditions in the Koelle method. In: *Biblioteca Anatomy*, 2. Karger, Basel, pp. 11–20.
- Logothetis, N.K., Eschenko, O., Murayama, Y., Augath, M., Steudel, T., Evrard, H.C., ..., Oeltermann, A., 2012. Hippocampal-cortical interaction during periods of subcortical silence. *Nature* 491 (7425), 547–553. doi:10.1038/nature11618.
- Logothetis, N.K., Augath, M., Murayama, Y., Rauch, A., Sultan, F., Goense, J., ..., Merkle, H., 2010. The effects of electrical microstimulation on cortical signal propagation. *Nat. Neurosci.* 13 (10), 1283–1291. doi:10.1038/nn.2631.
- Logothetis, N.K., Guggenberger, H., Peled, S., Pauls, J., 1999. Functional imaging of the monkey brain. *Nat. Neurosci.* 2, 555–562.
- Mai, J.K., Forutan, F., 2012. Thalamus. In: Mai, J.K., Paxinos, G. (Eds.), *The Human Nervous System*, third ed. Academic Press.
- Mai, J.K., Paxinos, G., 2012. *The Human Nervous System*, third ed. Academic Press.
- Manera, A.L., Dadar, M., Collins, D.L., Ducharme, S. Frontotemporal Lobar Degeneration Neuroimaging Initiative, 2019. Deformation based morphometry study of longitudinal MRI changes in behavioral variant frontotemporal dementia. *NeuroImage Clin.* 24, 10209.
- Mantini, D., Hasson, U., Bett, V., Perrucci, M.G., Romani, G.L., Corbetta, M., Orban, G.A., Vanduffel, W., 2012. Interspecies activity correlations reveal functional correspondence between monkey and human brain areas. *Nat. Methods* 9 (3), 277–282. doi:10.1038/nmeth.1868.
- Martin, R.F., Bowden, D.M., 2000. *Primate Brain Maps: Structure of the Macaque Brain*. Elsevier Science University of Washington, U.S.A.
- Milham, M., Petkov, C.I., Margulies, D.S., Schroeder, C.E., Bassi, M.A., Belin, P., Fair, D.A., Fox, A., Kastner, S., Mars, R.B., Messinger, A., Poirier, C., Vanduffel, W., Van Essen, D.C., Alvand, A., Becker, Y., Ben Hamed, S., Benn, A., Bodin, C., Boretius, S., Cagna, B., Coulon, O., El-Gohary, S.H., Evrard, H., Farkel, S.J., Friedrich, P., Froudrist-Walsh, S., Garza-Villarreal, E.A., Gao, Y., Gozzi, A., Grigis, A., Hartig, R., Hayashi, T., Heuer, K., Howells, H., Ardesch, D.J., Jarraya, B., Jarrett, W., Jedema, H.P., Kagan, I., Kelly, C., Kennedy, H., Klink, P.C., Kwok, S.C., Leech, R., Liu, X., Madan, C., Madushanka, W., Majka, P., Mallon, A.-M., Marche, K., Meguerditchian, A., Menon, R.S., Merchant, H., Mitchell, A., Nenning, K.-H., Nikolaidis, A., Ortiz-Rios, M., Pagani, M., Pareek, V., Prescott, M., Procyk, E., Rajimehr, R., Rautu, I.-S., Raz, A., Roe, A.W., Rossi-Pool, R., Roumazelles, L., Sakai, T., Sallet, J., García-Saldivar, P., Sato, C., Sawiak, S., Schiffer, M., Schwedzirk, C.M., Seidlitz, J., Sein, J., Shen, Z., Shmuel, A., Silva, A.C., Simone, L., Sirmplatz, N., Sliwa, J., Smallwood, J., Tasserie, J., Thiebaut de Schotten, M., Toro, R., Trapeau, R., Uhrig, L., Vezoli, J., Wang, Z., Wells, S., Williams, B., Xu, T., Xu, A.G., Yacoub, E., Zhan, M., Ai, L., Amiez, C., Balezeau, F., Baxter, M.G., Blezer, E.L.A., Brochier, T., Chen, A., Croxson, P.L., Damatac, C.G., Dehaene, S., Everling, S., Fleysher, L., Freiwald, W., Griffiths, T.D., Guedj, C., Hadj-Bouziane, F., Harel, N., Hiba, B., Jung, B., Koo, B., Laland, K.N., Leopold, D.A., Lindenfors, P., Meunier, M., Mok, K., Morrison, J.H., Nacef, J., Nagy, J., Pinsky, M., Reader, S.M., Roelfsema, P.R., Rudko, D.A., Rushworth, M.F.S., Russ, B.E., Schmid, M.C., Sullivan, E.L., Thiele, A., Todorov, O.S., Tsao, D., Ungerleider, L., Wilson, C.R.E., Ye, F.Q., Zarco, W., Zhou, Y., 2020. Accelerating the evolution of nonhuman primate neuroimaging. *Neuron* 105, 600–603 doi.org/10/ggvm7d.
- Messinger, A., Sirmplatz, N., Heuer, K., Loh, K.K., Mars, R.B., Sein, J., Xu, T., Glen, D., Jung, B., Seidlitz, J., Taylor, P., Toro, R., Garza-Villarreal, E.A., Sponheim, C., Wang, X., Benn, R.A., Cagna, B., Dadarwal, R., Evrard, H.C., Garcia-Saldivar, P., Giavasis, S., Hartig, R., Lepage, C., Liu, C., Majka, P., Merchant, H., Milham, M.P., Rosa, M.G.P., Tasserie, J., Uhrig, L., Margulies, D.S., Klink, P.C. A collaborative resource platform for non-human primate neuroimaging: this issue. *Neuroimage* 226:117519. doi:10.1016/j.neuroimage.2020.117519.
- Milham, M.P., Ai, L., Koo, B., Xu, T., Amiez, C., Balezeau, F., Baxter, M.G., Blezer, E.L.A., Brochier, T., Chen, A., Croxson, P.L., Damatac, C.G., Dehaene, S., Everling, S., Fair, D.A., Fleysher, L., Freiwald, W., Froudrist-Walsh, S., Griffiths, T.D., Guedj, C., Hadj-Bouziane, F., Ben Hamed, S., Harel, N., Hiba, B., Jarraya, B., Jung, B., Kastner, S., Klink, P.C., Kwok, S.C., Laland, K.N., Leopold, D.A., Lindenfors, P., Mars, R.B., Menon, R.S., Messinger, A., Meunier, M., Mok, K., Morrison, J.H., Nacef, J., Nagy, J., Rios, M.O., Petkov, C.I., Pinsky, M., Poirier, C., Procyk, E., Rajimehr, R., Reader, S.M., Roelfsema, P.R., Rudko, D.A., Rushworth, M.F.S., Russ, B.E., Sallet, J., Schmid, M.C., Schwedzirk, C.M., Seidlitz, J., Sein, J., Shmuel, A., Sullivan, E.L., Ungerleider, L., Thiele, A., Todorov, O.S., Tsao, D., Wang, Z., Wilson, C.R.E., Yacoub, E., Ye, F.Q., Zarco, W., Zhou, Y., Margulies, D.S., Schroeder, C.E., 2018. An Open Resource for Non-human Primate Imaging. *Neuron* 100, 61–74 e2. doi.org/10/gffxtm.
- Moirano, J.M., Bezgin, G.Y., Ahlers, E.O., Kötter, R., Converse, A.K., 2019. Rhesus macaque brain atlas regions aligned to an MRI template. *Neuroinformatics* 17, 295–306.
- Molfese, P.J., Glen, D., Mesite, L., Cox, R.W., Hoeft, F., Frost, S.J., Mencl, W.E., Pugh, K., & Bandettini, P.A. (Accepted). The Haskins pediatric atlas: An MRI-based pediatric template and atlas. *Pediatric Radiology*.
- Murris, S.R., Arsenault, J.T., Vanduffel, W., 2020. Frequency- and state-dependent network effects of electrical stimulation targeting the ventral tegmental area in macaques. *Cereb. Cortex* 00, 1–16. doi:10.1093/cercor/bhaa007.
- Nassi, J.J., Avery, M.C., Cetin, A.H., Roe, A.W., Reynolds, J.H., 2015. Optogenetic activation of normalization in alert macaque visual cortex. *Neuron* 86 (6), 1504–1517. doi:10.1016/j.neuron.2015.05.040.
- Noonan, M.P., Sallet, J., Mars, R.B., Neubert, F.X., O'Reilly, J.X., Andersson, J.L., Mitchell, A.S., Bell, A.H., Miller, K.L., Rushworth, M.F.S., 2014. A neural circuit covariety with social hierarchy in macaques. *PLoS Biol.* 12 (9), e1001940. doi:10.1371/journal.pbio.1001940.
- Oler, J.A., Birn, R.M., Patriat, R., Fox, A.S., Shelton, S.E., Burghy, C.A., Stodola, D.E., Essex, M.J., Davidson, R.J., Kalin, N.H., 2012. Evidence for coordinated functional activity within the extended amygdala of non-human and human primates. *NeuroImage* 61, 1059–1066. doi:10.1016/j.neuroimage.2012.03.045, pmid:22465841.
- Olszewski, J., 1952. *The Thalamus of the Macaca Mulatta: An Atlas for Use with the Stereotaxic Instrument*. Karger, New York.
- Ongur, D., An, X., Price, J.L., 1998. Prefrontal cortical projections to the hypothalamus in macaque monkeys. *J. Comp. Neurol.* 401 (4), 480–505.
- Ortiz-Rios, M., Kusmierenk, P., DeWitt, I., Archakov, D., Azevedo, F.A.C., Sams, M., Jaaskelainen, I.P., Keliris, G.A., Rauschecker, J.P., 2015. Functional MRI of the vocalization-processing network in the macaque brain. *Front. Neurosci.* 9, 113. doi:10.3389/fnins.2015.00113.
- Pauli, W.M., Nili, A.N., Tyszka, J.M., 2018. A high-resolution probabilistic *in vivo* atlas of human subcortical brain nuclei. *Sci. Data* 5, 180063.
- Paxinos, G., Huang, X.-F., Petrides, M., Toga, A.W., 2009. *The Rhesus Monkey Brain in Stereotaxic Coordinates*, second ed. Elsevier Academic Press, San Diego, U.S.A.
- Paxinos, G., Petrides, M., Evrard, H.C., in preparation. The Rhesus Monkey Brain in Stereotaxic Coordinates. fourth ed. Elsevier. <https://www.elsevier.com/books/the-rhesus-monkey-brain-in-stereotaxic-coordinates/paxinos/978-0-12-815852-4>.
- Pipitone, J., Park, M.T.M., Winterburn, J., Lett, T.A., Lerch, J.P., Pruessner, J.C., Lepage, M., Voineskos, A.N., Chakravarty, M.M. the Alzheimer's Disease Neuroimaging Initiative, 2014. Multi-atlas segmentation of the whole hippocampus and subfields using multiple automatically generated templates. *NeuroImage* 101, 494–512.
- Puelles, L., Harrison, M., Paxinos, G., Watson, C., 2013. A developmental ontology for the mammalian brain based on the prosomeric model. *Trends Neurosci.* 36, 570–578.
- Quan, Z., Gao, Y., Qu, S., Wang, X., Friedman, R.M., Chernov, M.M., Kroenke, C.D., Roe, A.W., Zhang, X., 2020. A 16-channel loop array for *in vivo* macaque whole-brain imaging at 3 T. *Magn. Reson. Imaging* 68, 167–172.
- Rapan, L., Froudrist-Walsh, S., Niu, M., Xu, T., Funck, T., Zilles, K., Palomero-Gallagher, N., 2021. Multimodal 3D atlas of the macaque monkey motor and premotor cortex. *NeuroImage* 226, 117574.
- Reveley, C., Gruslys, A., Ye, F.Q., Glen, D., Samaha, J., Russ, B.E., ..., Saleem, K.S., 2017. Three-dimensional digital template atlas of the macaque brain. *Cereb. Cortex* 1–15. doi:10.1093/cercor/bhw248.
- Rohlfing, T., Kroenke, C.D., Sullivan, E.V., Dubach, M.F., Bowden, D.M., Grant, K.A., Pfefferbaum, A., 2012. The INIA19 template and neuromaps atlas for primate brain image parcellation and spatial normalization. *Front. Neuroinformatics* 6, 27. doi:10.3389/fninf.2012.00027.
- Saad, Z.S., Reynolds, R.C., Argall, B., Japee, S., Cox, R.W., 2004. SUMA: an interface for surface-based intra- and inter-subject analysis with AFNI. In: 2nd IEEE International Symposium on Biomedical Imaging: Nano to Macro (IEEE Cat No. 04EX821), 2, pp. 1510–1513. doi:10.1109/ISBI.2004.1398837.
- Saad, Z.S., Glen, D.R., Chen, G., Beauchamp, M.S., Desai, R., Cox, R.W., 2009. A new method for improving functional-to-structural MRI alignment using local Pearson correlation. *NeuroImage* 44, 839–848. doi:10.1016/j.neuroimage.2008.09.037.
- Saleem, K.S., Logothetis, N.K., 2012. *A Combined MRI and Histology Atlas of the Rhesus Monkey Brain in Stereotaxic Coordinates*, second ed. Academic Press.
- Saper, C.J., 2012. Hypothalamus. In: Mai, J.K., Paxinos, G. (Eds.), *The Human Nervous System*, third ed. Academic Press.
- Seidlitz, J., Sponheim, C., Glen, D., Ye, F.Q., Saleem, K.S., Leopold, D.A., Ungerleider, L., Messinger, A., 2018. A population MRI brain template and analysis tools for the macaque. *NeuroImage* 170, 121–131. doi:10.1016/j.neuroimage.2017.04.063.
- Sørensen, T., 1948. A method of establishing groups of equal amplitude in plant sociology based on similarity of species and its application to analyses of the vegetation on Danish commons. *Kongelige Danske Videnskabernes Selskab* 5 (4), 1–34.
- Stauffer, W.R., Lak, A., Yang, A., Borel, M., Paulsen, O., Boyden, E.S., Schultz, W., 2016. Dopamine neuron-specific optogenetic stimulation in rhesus macaques. *Cell* 166 (6), 1564–1571 e6.
- Stefanacci, L., Amaral, D.G., 2000. Topographic organization of cortical inputs to the lateral nucleus of the macaque monkey amygdala: a retrograde tracing study. *J. Comp. Neurol.* 421 (1), 52–79.
- Strange, B.A., Witter, M.P., Lein, E.S., Moser, E.I., 2014. Functional organization of the hippocampal longitudinal axis. *Nat. Rev. Neurosci.* 15, 655–669.
- Tustison, N.J., Avants, B.B., Cook, P.A., Zheng, Y., Egan, A., Yushkevich, P.A., Gee, J.C., 2010. N4ITK: improved N3 bias correction. *IEEE Trans. Med. Imaging* 29 (6), 1310–1320.
- Wells, A.M., Garcia-Cabezas, M.A., Barbas, H., 2020. Topological atlas of the hypothalamus in adult rhesus monkey. *Brain Struct. Funct.* 225 (6), 1777–1803. doi:10.1007/s00429-020-02093-8.
- Xu, T., Sturgeon, D., Ramirez, J.S.B., Froudrist-Walsh, S., Margulies, D.S., Schroeder, C.E., Fair, D.A., Milham, M.P., 2019. Interindividual variability of functional connectivity in awake and anesthetized rhesus macaque monkeys. *Biol. Psychiatry Cognit. Neurosci. Neuroimaging* 4, 543–553.
- Zakszewski, E., Adluru, N., Tromp, D.P.M., Kalin, N., Alexander, A.L., 2014. A diffusion-tensor-based white matter atlas for rhesus macaques. *PLoS One* 9, e107398.